

# Cooling performance of near-infrared and traditional high-reflective coatings under various coating modes and building area densities in 3D urban models: Scaled outdoor experiments

Jian Hang <sup>a</sup>, Mengrong Lu <sup>b,\*</sup>, Longhao Ren <sup>a</sup>, Hanying Dong <sup>a</sup>, Yuguang Zhao <sup>c,d,e</sup>, Na Zhao <sup>c,d,e</sup>

<sup>a</sup> School of Atmospheric Sciences, Sun Yat-sen University, and Southern Marine Science and Engineering Guangdong Laboratory (Zhuhai), Zhuhai, China

<sup>b</sup> Integrated Research on Energy, Environment and Society (IRES), Energy and Sustainability Research Institute Groningen, University of Groningen, Groningen, 9747 AG, the Netherlands

<sup>c</sup> Hebei Key Laboratory of Meteorology and Ecological Environment, Hebei province, China

<sup>d</sup> Xingtai Atmospheric Environment Field Scientific Test Base of CMA, Hebei province, China

<sup>e</sup> Hebei Meteorological Disaster Prevention and Environment Meteorology Center, Hebei province, China



## ARTICLE INFO

### Keywords:

Scaled outdoor experiments  
Cool roof/wall  
Building area density  
Near-infrared reflective (NIR) coating  
Albedo  
High-reflective cool materials

## ABSTRACT

The urban heat island can be mitigated by using surface cool coatings. However, it is challenged to conduct field measurements in real cities for quantifying the integrated effects of urban geometries and cool coatings on urban thermal environments. We conducted scaled outdoor experiments of 3D urban models(building height  $H = 1.2$  m, street width  $W = 0.5$  m/0.25 m) during May-July 2023 in a subtropical city(Guangzhou). Significant urban parameters including two plan area index( $\lambda_p=0.25/0.44$ ), three cool materials of traditional white/yellow coatings(TR-W, TR-Y with reflectance: 0.73, 0.76) and near-infrared reflective yellow coating(NIR-Y, 0.76, 0.92 in the near-infrared spectrum), and three coating modes(only roof, R-type; only vertical walls, W-type; both roof and walls, RW-type) were considered.

In uncoated cases, overall average urban albedo  $\alpha_a = 0.13/0.16$  when  $\lambda_p=0.25/0.44$ . Under TR-W coatings,  $\lambda_p=0.44$  experienced greater  $\alpha_a$  than  $\lambda_p=0.25$ , and all three coating modes significantly enhanced  $\alpha_a$ , with more effective by R-type and RW-type. Moreover, at  $\lambda_p=0.44$ , average wall/indoor cooling effects of W-type and RW-type were  $0.6\text{--}1.6^\circ\text{C}/0.7\text{--}1.6^\circ\text{C}$ , less than those at  $\lambda_p=0.25(2.3\text{--}4.4^\circ\text{C}/2.3\text{--}3.8^\circ\text{C})$  with a larger sky view factor. As  $\lambda_p$  changing from 0.25 to 0.44, the overall urban heat storage flux( $\Delta Q_S$ ) significantly rose, whereas cool coatings had little influence on  $\Delta Q_S$ . Besides, the NIR coating increased  $\alpha_a$  to  $0.28/0.47$  under W-type/RW-type, which was an increase of 33.3 %/30.6 % compared to the TR-W coating, and reduced  $\langle \Delta T_{wall} \rangle(0.9\text{--}1.3^\circ\text{C}/2.2\text{--}2.5^\circ\text{C}$  for W-/RW-type) by 125–225 %, and  $\langle \Delta T_{indoor\_air} \rangle(1.4^\circ\text{C}/2.9^\circ\text{C})$  by 55.6 %–61.1 % more than TR-Y ( $0.9^\circ\text{C}/1.8^\circ\text{C}$ ). Street air temperature showed minimal change with cool coatings. These experiments can validate and improve numerical simulations, providing a scientific basis for urban planning.

## 1. Introduction

Accelerated urbanization has resulted in the emergence of higher and denser city buildings, alongside the rapid gathering urban population (Pisello, 2017; United Nations Human Settlements Programme (UN-Habitat) 2020). In urban areas, irregular and high-density structures, along with materials of high heat capacity and low reflectivity, reduce the overall urban albedo, moreover the lack of green spaces and prevalence of impermeable surfaces, thereby enhances solar radiation

capture/thermal storage and reduces latent heat flux (Oke et al., 1991). These factors directly or indirectly lead to the Urban Heat Island (UHI) effect with elevated urban air and surface temperatures than rural areas (Santamouris, 2015, 2016; Zhang et al., 2024). Under global warming, the UHI effect significantly raises the incidence and mortality rates of heat-related illnesses (Donateo et al., 2023; Paravantis et al., 2017; Santamouris, 2015a) and energy demand for summer cooling in cities (Rincón et al., 2024), particularly during extreme weather conditions such as heatwaves.

\* Corresponding author.

E-mail address: [m.lu@rug.nl](mailto:m.lu@rug.nl) (M. Lu).

Nomenclature	
$B$	Length and width of building model (m)
$D$	Diffusivity ( $\text{mm}^2 \text{s}^{-1}$ )
$e$	Emissivity
$H$	Height of building models (m)
$H/W$	Aspect ratio
$G$	Terrestrial global solar radiation on a horizontal surface ( $\text{W m}^{-2}$ )
$G_0$	Extraterrestrial solar radiation at the top of the atmosphere ( $\text{W m}^{-2}$ )
$I_{sc}$	Solar constant ( $1367 \text{ W m}^{-2}$ )
$i$	Basic elements in urban volume, including building wall, roof, ground, street and indoor air
$k$	Conductivity ( $\text{W m}^{-1} \text{ K}^{-1}$ )
$K_t$	Clearness index
$N$	Day number in the year ( $N = 1$ and $N = 365$ is the first and the last day in the year respectively)
$Q^*$	Net radiation ( $\text{W m}^{-2}$ )
$Q_F$	Anthropogenic heat ( $\text{W m}^{-2}$ ) $\Delta Q_S$ Heat storage ( $\text{W m}^{-2}$ )
$Q^*_{\text{max}}/Q^*_{\text{avg}}$ , $\Delta Q_S_{\text{max}}/\Delta Q_S_{\text{avg}}$	Maximum/Average net radiation and heat storage ( $\text{W m}^{-2}$ ) during the daytime (6:00–18:00)
$Q_H$	Sensible heat ( $\text{W m}^{-2}$ )
$Q_E$	Latent heat ( $\text{W m}^{-2}$ )
$\Delta Q_A$	Net advective heat flux ( $\text{W m}^{-2}$ )
$Q_{K\uparrow}, Q_{K\downarrow}$	$(K\uparrow), (K\downarrow)$ Upward ( $\uparrow$ ) and downward ( $\downarrow$ ) shortwave radiation ( $\text{W m}^{-2}$ )
$Q_{L\uparrow}, Q_{L\downarrow}$	Upward ( $\uparrow$ ) and downward ( $\downarrow$ ) longwave radiation ( $\text{W m}^{-2}$ )
$Q_{K\downarrow}$	Average downward shortwave radiation during the daytime (6:00–18:00)
$Re$	Reynolds Numbers
$S$	Volumetric heat capacity ( $\text{J m}^{-3} \text{ K}^{-1}$ )
$T_{\text{coated}}, T_{\text{uncoated}}$	Temperature of coated and uncoated cases
$T_{\text{east wall}}, T_{\text{west wall}}, T_{\text{south wall}}, T_{\text{north wall}}$	East/West/South/North wall surface temperature ( $^{\circ}\text{C}$ )
$T_{\text{roof}}, T_{\text{ceiling}}, T_{\text{ground}}$	Rooftop/ceiling/ground surface temperature
$T_{\text{indoor air}}, T_{\text{street air}}$	Indoor/street air temperature
$\Delta T_{\text{max}}/\Delta T_{\text{min}}$	Maximum/minimum temperature difference
$\Delta T$	Temperature difference between coated and uncoated cases
$T^-$ , $\langle T \rangle$	Temporally/Spatially averaged temperature
$\Delta T/\Delta t$	Rate of temperature change over a given period ( $\text{K s}^{-1}$ )
TR-W, TR-Y, NIR-Y	Traditional reflective white, yellow coating and near-infrared reflective yellow coating
$W$	Street width (m)
$z$	Height of measurement (m)
$\alpha$	Albedo
$\alpha_s$	Instantaneous albedo
$\alpha_a$	Average albedo of a specific period
$\lambda_p, \lambda_f$	Building area density or plan area index, frontal area density
$\rho$	Density ( $\text{g cm}^{-3}$ )
$\omega$	Sunrise/sunset hour angle in degrees, and the sunrise hour angle is the negative of the sunset hour angle
$\delta$	Solar declination angle
$\phi$	Latitude of the location in degrees
$\Phi$	Diameter of thermocouple (mm)

### 1.1. Literature review of numerical and experimental studies on cool coatings

Using cool coating with high reflectivity and emissivity at building envelopes and road surfaces is widely recognized as a cost-effective passive cooling strategy in cities (Family et al., 2017; Raman et al., 2014; Santamouris et al., 2011). Over the last decade, numerous simulations have consistently verified that cool roofs or walls significantly contribute to the reduction of urban air and surface temperatures as well as energy consumption across scales from local neighborhoods and buildings (Li et al., 2024; Zingre et al., 2015) to urban districts (Chen & Lu, 2021a; Nazarian et al., 2019; Zhang et al., 2017) and the regional-scale or global-scale environments (Jacobson et al., 2012).

These simulations often lack experimental data for coated scenarios or are influenced by other variables, such as climate zones, urban morphology, and cool materials, making direct comparison or validation difficult. The high-quality, parameterized field experiments in urban environments are essential for validating numerical models related to urban climate. However, most such studies focus on applying cool materials to individual buildings or rooms. Research in different climate zones, such as the Mediterranean (Pisello et al., 2014) and tropical (Garg et al., 2016) and subtropical (Kim et al., 2020) climate, has shown that cool roofs can reduce roof temperatures by 10 to 25 °C, leading to indoor cooling of about 3 °C. Additionally, Donthu et al. (2024) demonstrated that cool canyons could reduce street air temperatures by up to 2 °C. These studies underscore the effectiveness of cool roofs and walls in

**Table 1**

Summary of previous scaled outdoor experiments on the effect of cool roofs and walls.

Author	2D/ 3D	Coating mode	Location/ Climate zone	Coating material	Main finding
Doya et al., 2012	2D	W-type (only vertical walls)	France/Temperate marine climate	NIR coating (Solar reflectance, 0.38)	Surface cooling: up to 1.5 °C Indoor air cooling: up to 2.5 °C
Morini et al., 2018	2D	W-type	Perugia, Italy/Humid subtropical climate	White coating (0.85)	Cooling effects were most pronounced at $H/W = 0.5$
Lu et al., 2023	3D	R-type (only roof), W-type, RW-type (both roof and walls)	Guangzhou, P.R. China/Subtropical monsoon climate	White coating (0.73)	Wall cooling: up to 2.0 °C Street air cooling: up to 1.2 °C
He et al., 2020	3D	R-type	Shanghai, P.R. China/Subtropical monsoon climate	White coating (0.7)	Roof cooling: average cooling effect of 3.3 °C in summer
Wang et al., 2022	3D	RW-type	Qingdao, P.R. China/Temperate monsoon climate	Retro-reflective (RR) and high reflective (HR) materials (~0.5 and ~0.8)	Indoor air cooling: RR-coating was 2.3 °C cooler than HR-coating.
Xu et al., 2024	3D	R-type, W-type, RW-type	Guangzhou, P.R. China/Subtropical monsoon climate	White coating (0.86)	Roof surface: up to 13.5 °C Indoor air cooling: up to 3.9 °C
Wang et al., 2024	3D	W-type	Guangzhou, P.R. China/Subtropical monsoon climate	White coating (0.86)	Indoor air cooling: up to 4.5 °C
Revel et al., 2014a	3D	R-type, W-type	Algete, Spain/mix of Mediterranean and Continental climate	Green coating (0.42)	Heat flux reduction: up to 10.2 $\text{W m}^{-2}$

urban buildings under various climatic conditions. But it is still challenging and expensive to conduct cool wall experiments in realistic urban districts or entire cities.

Scaled outdoor experiments can provide enhanced control in configuring building parameters and mitigating unrelated urban factors (Table 1). This approach can carry out detailed parametric analyses of thermal dynamics, and energy fluxes in real-world weather conditions (Chen et al., 2020b; Kanda, 2006; Kawai et al., 2010). Street-scale experiments with cool coatings, primarily in two-dimensional (2D) street canyons, have shown that cool walls enhance indoor thermal comfort by approximately 1.5 °C for walls and 2.5 °C indoors during peak summer (Doya et al., 2012). Morini et al. (2018) further explored the performance of high-albedo wall coatings under different aspect ratios, finding that they caused a warming effect on the ground surface in narrow canyons ( $H/W = 2$ ) but provided greater cooling benefits in wider canyons ( $H/W = 0.5$ ). At the three-dimensional scale, many studies have demonstrated the impact of applying cool coatings to individual scaled buildings in hot regions, using short-term measurements to validate and develop models for predicting roof thermal performance (Chen et al., 2021b; Jiang et al., 2023). However, the complex interactions between buildings, such as shading effects, are often overlooked in single-building scaled experiments (Xu et al., 2023). In recent years, the Scaled Outdoor Measurement of Urban Climate and Health (SOMUCH) platform has been established (Chen et al., 2020a, 2020b; Chen et al., 2021; Hang & Chen, 2022; Xu et al., 2024). Our recent research (Lu et al., 2023) investigated the effects of high-reflective roofs and walls in three-dimensional (3D) building clusters within a subtropical region using 25 concrete scaled models arranged in a  $5 \times 5$  configuration. Under medium building area density ( $\lambda_p = 0.44$ ), cool coatings applied to both roofs and vertical walls reduced surface temperatures by over 8 °C and decreased street canyon air temperatures by up to 1.2 °C. Wang et al. (2024) also tested cool walls on a scaled multi-story building (height  $H = 1.2$  m) and found a significant reduction in average indoor air temperatures on each floor, with a maximum difference of 4.5 °C. Despite these findings, there is still limited research comparing the effectiveness of cool roofs and walls in building clusters under varying urban densities and with different types of cool materials.

With advancements in cool materials, a growing number of innovative materials with unique optical or thermodynamic properties have been developed, including retro-reflective materials (Wang et al., 2022), phase change materials (Lei et al., 2017), super cool materials like scalable broadband radiative coolers (Feng et al., 2021; Santamouris et al., 2020), and near-infrared reflective coatings (Coser et al., 2015), which enhance reflectivity in the near-infrared spectrum that constitutes nearly half of solar radiation energy. Most experiments on these materials have been conducted in laboratories (Revel et al., 2014) or on outdoor flat surfaces (Becherini et al., 2018; Pisello et al., 2016). However, high-quality experimental data under real weather conditions and building structures are still needed. Scaled outdoor experiments offer a practical approach to assess the performance of these materials in specific architectural layouts at relatively lower costs.

Besides, to better understand the impact of cool coatings on the urban surface energy balance (SEB), it is essential to investigate their effect on building thermal storage (Wang et al., 2021). However, measuring heat flux in real urban settings, especially in dense city centers, is challenging due to complex urban morphology, and direct measurement of building heat storage is not feasible. In scaled outdoor experiments, thermal storage can be estimated using the element surface temperature method (ESTM, Offerle et al., 2005), with minimal anthropogenic heat influence. Revel et al. (2014a) conducted research in a mixed Mediterranean-Continental climate using medium-scale mock-ups ( $2.4 \times 3 \times 2.4$  m $^3$ ) with main building components (windows, door and ventilation). They found that increasing wall solar reflectance from 0.25 to 0.42 using a cool green coating reduced peak heat flux by  $10.2$  W m $^{-2}$ , a 50 % relative decrease. Despite these insights, using scaled models to evaluate cool coatings' effects on building

thermal storage remains rare, particularly in high-rise, densely built environments.

## 1.2. Objectives of the study

Overall, to address the gap, we executed scaled outdoor experiments in Guangzhou, China, a region characterized by a typical subtropical monsoon climate. During the hot summer in 2023, from May 11 to Jul 12, we delved into the quantitative effect of different coating materials (TR-W, TR-Y and NIR-Y) and coating modes (uncoated, R-type, W-type and RW-type) across two building area densities ( $\lambda_p = 0.25, 0.44$ ) on the indoor and outdoor thermal environment in three-dimensional building clusters.

Our investigation revolved around two primary concerns:

- (1). the cooling benefits of cool coatings under different coating modes in two building layouts ( $\lambda_p = 0.25, 0.44$ );
- (2). a comparison of the cooling benefits between traditional high-reflectance coating and near-infrared reflective coating in a dense building layout ( $\lambda_p = 0.44$ ).

The findings provide reliable, high-quality experimental data to support diverse reflective cooling strategies for mitigating urban overheating, particularly in high-rise and dense building areas. Moreover, this study could also provide a reference for analyzing the effectiveness of cool coatings, such as cool roofs, on heat storage flux and indoor thermal comfort under specific climatic conditions (subtropical hot and humid climates). Additionally, the data from these experiments can also be utilized to validate corresponding numerical simulations.

## 2. Methodology

### 2.1. Study site

We conducted this study in the Scaled Outdoor Measurement of Urban Climate and Health (SOMUCH) platform, located in the suburb of Guangzhou, China (23°1'N, 113°25'E). Guangzhou has a humid subtropical climate, with hot, humid summers and distinct seasonal features. From 1981 to 2010, the highest monthly temperature was 29.4 °C in July, and the lowest was 14.1 °C in January, with annual rainfall averaging 1801 mm (National Meteorological Information Center, <http://data.cma.cn/>). Long, hot summers and short, warm winters contribute to prolonged urban heat island effects, especially during summer (Hang et al., 2024b; Huang et al., 2010).

The SOMUCH platform covers an area of approximately 3000 m $^2$ , featuring a flat concrete surface with a thickness of around 0.2m. In our study, urban structures are simplified as concrete rectangular models (building width  $B = 0.5$  m, building height  $H = 1.2$  m), hollow inside with a wall thickness of 0.015 m, ensuring sufficient thermal inertia and detectable building thermal storage, as indicated in Table 2. All concrete building models are coated with grey coating at the beginning to maintain uniform surface colour, characterized by a generally low albedo and uniformly high emissivity.

This platform is set to use scaled urban canopy models to study urban climates. Past research has confirmed the platform's ability to acquire high-quality, high spatiotemporal resolution parametric field experimental data under realistic meteorological conditions. The geometric and dynamic similarity between the scaled model and the real world have been proved. Chen et al. (2020a) have tested the dynamic similarity of airflow by calculating the typical Reynolds Numbers ( $Re$ ) (Snyder, 1972) and validating the independence of the Reynolds number ( $Re \gg 11,000$ ) under typical background wind conditions in the SOMUCH experiment. After that, Chen et al. (2021) have examined the dynamic similarity of radiation by comparing the reflective short-wave radiation. In addition, Wang et al. (2021) have proved that the scaled building has sufficient thermal inertia and detectable building thermal

**Table 2**

Physical properties of all building model material.

Material	Density, $\rho$ (g cm $^{-3}$ )	Conductivity, $k$ (W m $^{-1}$ K $^{-1}$ )	Diffusivity, $D$ (mm $^2$ s $^{-1}$ )	Emissivity, $e$	Albedo, $\alpha$	Volumetric heat capacity, $S$ (J m $^{-3}$ K $^{-1}$ )
Concrete	2.42	2.073	1.386	0.87	0.24	$1.496 \times 10^6$

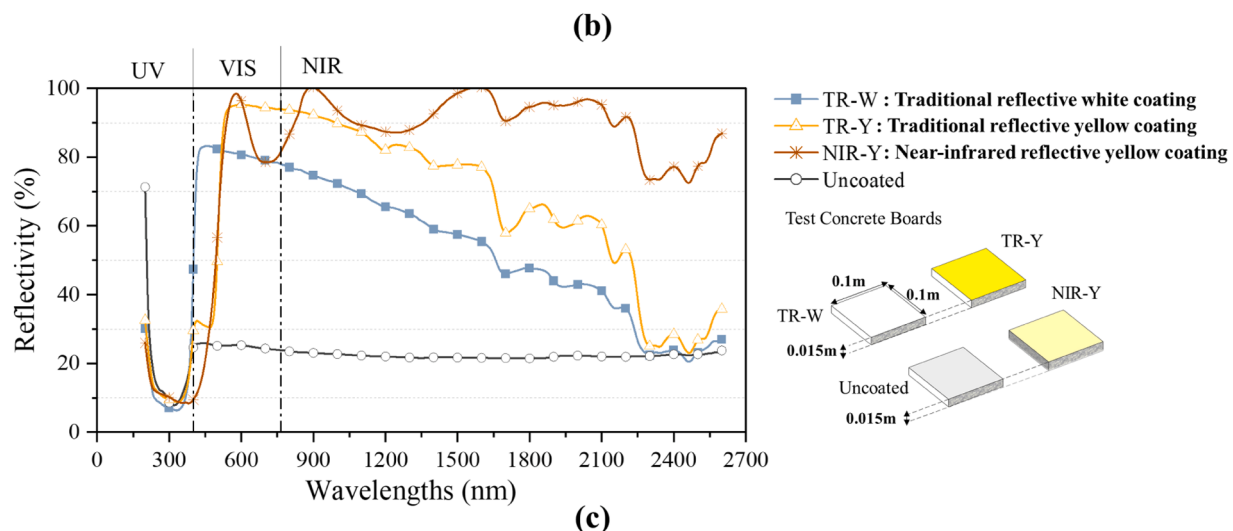
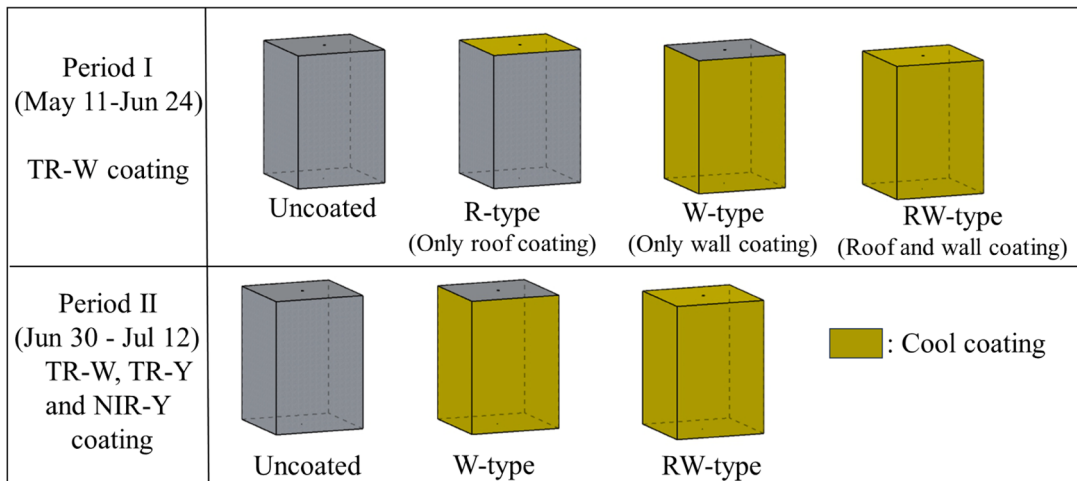
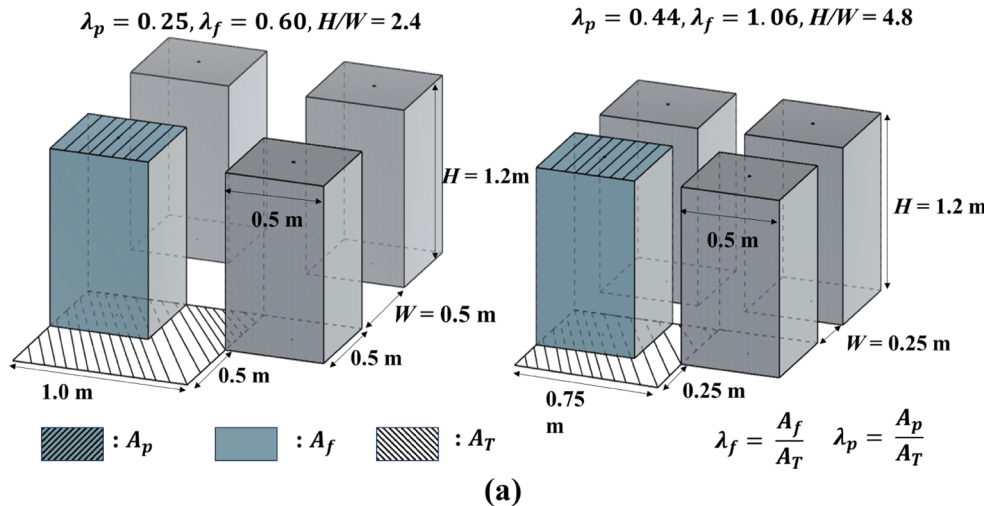


**Fig. 1.** Schematic of experimental settings: (a) different building area densities ( $\lambda_p = 0.25, 0.44$ ), (b) coating modes during two measurement periods, (c) the full band albedo of different coating concrete boards with a thickness of 0.015 m (UV: Ultraviolet Spectrum, VIS: Visible Spectrum, NIR: Near infrared Spectrum).

storage. The experiments in scaled street canyon or building clusters allow for parameter control to eliminate the impact of irrelevant variables like anthropogenic heat, which also permits consideration of the mutual shading and radiation reflection occurring between buildings in urban areas.

## 2.2. Experimental setup

The measurements were conducted from May 11 to Jul 12, 2023, a period characterized by the typical hot and humid conditions of subtropical climates. Throughout the Period I (May 11 - Jun 24) and II (Jun 30 - Jul 12), the average air temperatures were 27.8 °C and 30.8 °C, while the average relative humidity were 80.4 % and 83.61 %, respectively.

### 2.2.1. Setup for Period I (May 11 - Jun 24)

As illustrated in Fig. 1a and Fig. 2, we arranged four building clusters with two different building area densities (Plan area index  $\lambda_p = 0.25, 0.44$ , frontal area index  $\lambda_f = 0.60, 1.06$ ). These clusters consisted of 25 concrete blocks arranged in a 5-row 5-column configuration. For Period I, three white (TR-W) coating modes (R-type, W-type, RW-type) were considered as shown in Fig. 1b. We divided the four building clusters into two groups based on the plan area index ( $\lambda_p$ ) set to 0.25 and 0.44, corresponding to street widths ( $W$ ) of 0.5 m and 0.25 m, respectively. Each group included both a TR-W coating case and an uncoated case (only basic grey coating) as a baseline. Three coating modes (R-type, W-type and RW-type) were individually tested for a certain period (Table 3). To better eliminate the influence of environmental factors (e.g., rainfall, sky clearness index), we selected four days for in-depth analysis, including May 15, June 22, and May 28. Each characterized by similar sky clearness (sky clearness index,  $K_t$ ) and average daytime downward shortwave radiation ( $Q_{\text{K}\downarrow}$ ,  $\text{W m}^{-2}$ ), representing R-type, W-type, and RW-type coating scenarios, respectively. Notably, May 29 was chosen for comparison to observe the differential impacts of roof and wall coating (RW-type) cases under clearer weather conditions.

### 2.2.2. Setup for Period II (Jun 30 - Jul 12)

During Period II (Jun 30 - Jul 12), we adjusted the four building clusters to the same building area density ( $\lambda_p = 0.44$ ). Additionally, we

added two new coating materials - yellow coating (TR-Y) and yellow coating with a mixed mass fraction of 30 % near-infrared reflective (NIR) material (denoted as NIR-Y), which were compared with the TR-W coating. The reflectance and the emissivity of TR-W, TR-Y and NIR-Y coating boards were 0.73, 0.76 and 0.76, and 0.78, 0.94 and 0.92, respectively, as shown in Fig. 1c. With the addition of NIR material, the near-infrared reflectance of the yellow coating increased from 83 % to 92 %. From Jun 30 to Jul 6, we applied W-type doped with TR-W, TR-Y and NIR-Y coating to Areas (4), (2), and (1), respectively, while Area (3) remained uncoated as a control group. From Jun 8 to Jul 12, we changed the coating mode to RW-type. Two days (Jul 6, 12) are selected for analysis, and the corresponding weather conditions are shown in Table 3

In conclusion, this study investigates the effect of coating material, building area density, and coating mode on overall albedo, building surface cooling, indoor and street air temperature and building heat storage flux during two distinct periods:

- Period I emphasises on the effect of building area density ( $\lambda_p = 0.25$  and  $0.44$ ) and three TR-W coating modes (R-type, W-type, RW-type) (Section 3.1).
- Period II focuses the effect of coating material (TR-W, TR-Y and NIR-Y coating) applied in two modes (W-type, and RW-type) at  $\lambda_p = 0.44$  (Section 3.2).

## 2.3. Measurement setup

The field experiments in real urban areas are often challenging to acquire high-resolution measurement data, such as surface temperature. However, at SOMUCH platform, we have the capability to conduct detailed parameter measurements. The experiment measured various parameters, including the surface temperature of buildings, ground and sub-surface temperature, indoor and street air temperature and albedo. The detailed information of the corresponding measurement instruments is listed in Table 4.

### 2.3.1. Surface and air temperature measurement

Two kinds of thermocouples were utilised to measure surface and sub-surface temperature and air temperature. Specifically, the thermocouple with a diameter of 0.255 mm (TT-K-30-SLE) was employed to

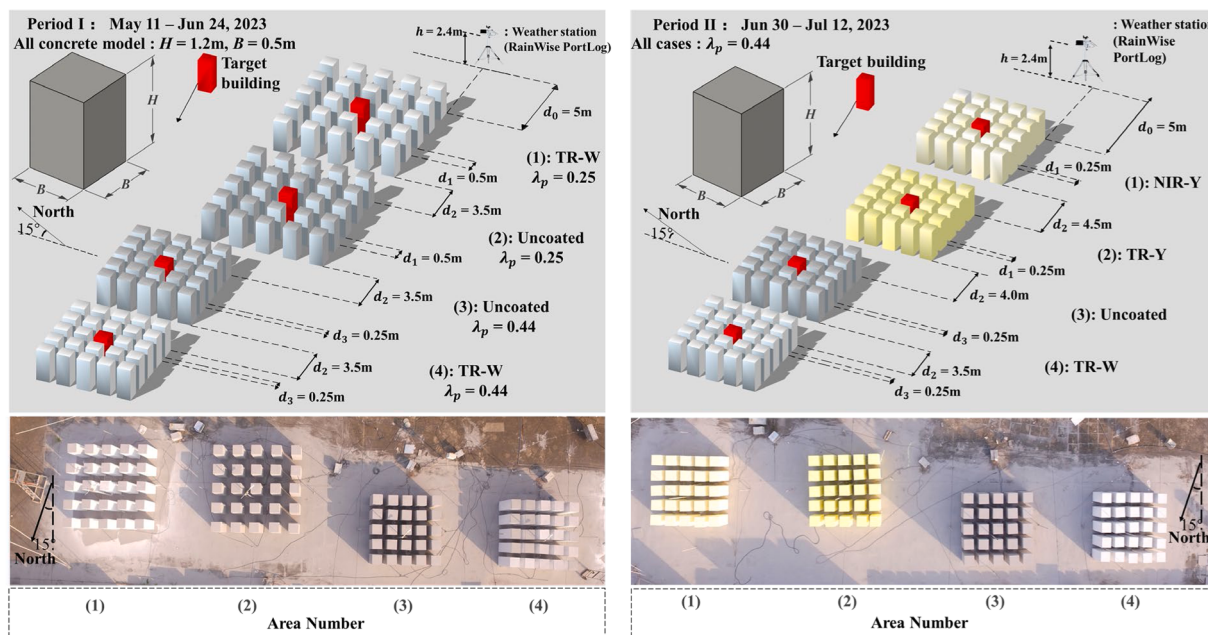


**Fig. 2.** Experimental set-up of scaled model outdoor field measurement and top view of four urban models for two periods: (a) Period I (May 11 to Jun 24, 2023), (b) Period II (Jun 30 to Jul 12, 2023).

**Table 3**

Overview of experiment settings and weather conditions for all investigated cases.

Coating mode	Coating material	Measurement period	Selected Date	Sky clearness index ( $K_t$ )	Plan area index ( $\lambda_p$ )	Ambient air range (°C)	Averaged downward shortwave radiation ( $\overline{Q_K \downarrow}$ , 6:00-18:00) (W m <sup>-2</sup> )	Averaged overall albedo, ( $\alpha_a$ , 6:00-18:00)	Case name	Area number Fig. 1	
Period I (May 11 to Jun 24)	R-type (only roof)	TR-W Coating	May 11 to May 19	May 15	0.53 (partially cloudy sky)	0.25, 0.44	19.8-31.9	461.9	0.32	[ $\lambda_p=0.44$ _R-type]	(4)
								0.16	[ $\lambda_p=0.44$ _Uncoated]	(3)	
								0.13	[ $\lambda_p=0.25$ _Uncoated]	(2)	
	RW-type (both roof and walls)		May 22 to May 30	May 28	0.49 (partially cloudy sky)	0.25, 0.44	26.2-35.8	462.6	0.24	[ $\lambda_p=0.25$ _R-type]	(1)
								0.36	[ $\lambda_p=0.44$ _RW-type]	(4)	
				May 29	0.63 (partially cloudy sky)	0.25, 0.44	26.3-37.1	563.1	0.16	[ $\lambda_p=0.44$ _Uncoated]	(3)
								0.14	[ $\lambda_p=0.25$ _Uncoated]	(2)	
								0.31	[ $\lambda_p=0.25$ _RW-type]	(1)	
	W-type (only vertical walls)		Jun 5 to Jun 24	Jun 22	0.50 (partially cloudy sky)	0.25, 0.44	27.7-36.5	443.7	0.17	[ $\lambda_p=0.44$ _W-type]	(4)
								0.15			
								0.32			
								0.20			
Period II (Jun 30 to Jul 12)	W-type	TR-W, TR-Y and NIR-Y coating	Jun 30 to Jul 6	Jul 7	0.63 (partially cloudy sky)	0.44	27.9-37.1	565.3	0.17	[ $\lambda_p=0.44$ _Uncoated]	(3)
								0.14	[ $\lambda_p=0.25$ _Uncoated]	(2)	
	RW-type		Jul 8 to Jul 12	Jul 12	0.60 (partially cloudy sky)	0.44	28.5-36.8	505.0	0.20	[ $\lambda_p=0.25$ _W-type]	(1)
								0.21	[TR-W_W-type]	(4)	
								0.18	[Uncoated]	(3)	
								0.26	[TR-Y_W-type]	(2)	
								0.28	[NIR-Y_W-type]	(1)	
								0.36	[TR-W_RW-type]	(4)	
								0.19	[Uncoated]	(3)	
								0.43	[TR-Y_RW-type]	(2)	
								0.47	[NIR-Y_RW-type]	(1)	

measure the surface temperature and the ground and sub-surface temperature. The arrangement of the instruments is displayed in Fig. 3b-d, where thermocouples were placed at five heights ( $z = 1.1, 0.9, 0.6, 0.3, 0.1$  m) on both the interior and exterior walls of four orientations of the central building. Four measurement points were set both on the interior (ceiling) and exterior roof. Moreover, three thermocouples were arranged on the eastern, southern street canyon centre and southeastern crossing on the ground. At the centre of the east street canyon, two measurement points were set at depths of 0.1 m, 0.2m. All exposed thermocouples were covered with aluminium foil tape to mitigate radiative interference (Yang & Li, 2009).

Regarding the air temperature, previous studies indicated that using thermocouples with the smaller diameter can reduce the interference from direct solar radiation (Pearlmutter et al., 2006; Syafii et al., 2017). To achieve high spatial resolution in air temperature observations, we employed exposed thermocouples with a diameter of 0.127 mm (TTK-36-SLE) to directly measure air temperature in the street canyon, with each measurement point fixed using 0.5 mm transparent nylon

fishing line. On the east and south street canyon, 0.05 m away from the building walls, and at the southeast street canyon centre, five thermocouples were arranged at different heights ( $z = 1.1, 0.9, 0.6, 0.3, 0.1$  m). We also positioned five air measurement points at various heights ( $z = 1.1, 0.9, 0.6, 0.3, 0.1$  m) inside the building to monitor indoor air temperature.

### 2.3.2. Other measurements

Four radiometers (CNR4 Net Radiometers) were used to measure downward/upward shortwave and longwave radiation ( $Q_K \downarrow$ ,  $Q_K \uparrow$ ,  $Q_L \downarrow$ ,  $Q_L \uparrow$ ) and were positioned at two different heights with varying building area densities (Fig. 3e). The radiometers were oriented in the north-south direction and were located at the centre of each 5 × 5 model. Besides, a weather station (Rainwise Portlog) was positioned 5 m east of the entire experimental site at a height of 2.4 m (twice the building height,  $2H$ ), as illustrated in Fig. 2. This station was utilized to measure background air temperature, rainfall, and relative humidity.

**Table 4**

Instruments for measurement: (Refer to Fig. 1, Fig. 2 and S1 for positions).

Measured parameter	Instrument	Sampling rate	Accuracy	Quantity
Background air temperature, rainfall, relative humidity, wind speed and direction	Weather station (Rainwise Portlog)	10 min	0.5 °C in range of −54–65 °C, 2 % at 25.4 mm h <sup>-1</sup> , 2 % from −40 °C to 65 °C, 2 % in range of 0–67 m s <sup>-1</sup> , 3° in range of 0–360°	1
Roof temperature	Thermocouples (Omega, TT-K30-SLE, Φ 0.255 mm)	3 s	1.1 °C or 0.4 % in range of −200–260 °C, refer to the greater one	16
Ceiling temperature	Thermocouples (Omega, TT-K30-SLE, Φ 0.255 mm)	3 s	1.1 °C or 0.4 % in range of −200–260 °C, refer to the greater one	16
Wall temperature	Thermocouples (Omega, TT-K30-SLE, Φ 0.255 mm)	3 s	1.1 °C or 0.4 % in range of −200–260 °C, refer to the greater one	160
Ground and sub-surface temperature	Thermocouples (Omega, TT-K30-SLE, Φ 0.255 mm)	3 s	1.1 °C or 0.4 % in range of −200–260 °C, refer to the greater one	36
Indoor and street air temperature	Thermocouples (Omega, TT-K36-SLE, Φ 0.127 mm)	3 s	1.1 °C or 0.4 % in range of −200–260 °C, refer to the greater one	92
Radiation balance ( $Q_{k\downarrow}$ , $Q_{k\uparrow}$ , $Q_{l\downarrow}$ , $Q_{l\uparrow}$ )	Radiometer (CNR4 Net Radiometer)	1 min	1 % in the range of 0 ~ 1000 w m <sup>-2</sup>	4

\*Note: The measuring component for the downward shortwave radiation flux ( $Q_{k\downarrow}$ ) of the radiometer in Area (1) is damaged. Therefore, we have substituted the measurements from the radiometer in the nearby Area (2) to calculate overall albedo.

## 2.4. Data processing

### 2.4.1. Surface energy balance (SEB)

According to Oke (1988), the energy balance equation was first defined as Eq. (1):

$$Q^* + Q_F = \Delta Q_S + Q_H + Q_E + \Delta Q_A \quad (1)$$

where  $Q^*$  is net radiation,  $Q_F$  is anthropogenic heat,  $\Delta Q_S$  is heat storage,  $Q_H$  is sensible heat,  $Q_E$  is latent heat, and  $\Delta Q_A$  is net advective heat flux. The unit of all terms in Eq. (1) are W m<sup>-2</sup>.  $Q^*$  can be calculated by downward/upward shortwave and longwave radiation ( $Q_{k\downarrow}$ ,  $Q_{k\uparrow}$ ,  $Q_{l\downarrow}$ ,  $Q_{l\uparrow}$ , W m<sup>-2</sup>) which is defined as:

$$Q^* = Q_{k\downarrow} - Q_{k\uparrow} + Q_{l\downarrow} - Q_{l\uparrow} \quad (2)$$

Here, the downward/upward shortwave and longwave radiation ( $Q_{k\downarrow}$ ,  $Q_{k\uparrow}$ ,  $Q_{l\downarrow}$ ,  $Q_{l\uparrow}$ , W m<sup>-2</sup>) were recorded continuously by CNR4 Net Radiometer at 1-minute intervals and would be used as 30-minute averages of the measured data.

In the SOMUCH platform, the terms  $Q_F$  and  $\Delta Q_A$  in Eq. (1) can be neglected due to the homogeneous geometry and material of the model setup, along with the absence of human activities. Therefore, Eq. (1) can be simplified to:

$$Q^* = \Delta Q_S + Q_H + Q_E \quad (3)$$

### 2.4.2. Building heat storage flux estimation

The heat flux ( $\Delta Q_S$ ) associated with storage represents thermal inertia and is often considered a crucial factor in the development of urban heat islands. Direct measurement of this flux in real urban areas is challenging (Grimmond et al., 1999). Offerle et al. (2005) introduced the Element Surface Temperature Method (ESTM), which simplified the 3D urban surface conceptually by breaking it down into one-dimensional elements for building walls, roofs, internal mass, and ground (Fig. 4). This method holds an advantage in that it calculates the  $\Delta Q_S$  in urban areas with minimal measurements of surface and air temperatures. The equation is as follows:

$$\Delta Q_S = \sum_i \frac{\Delta T}{\Delta t} s_i \Delta x_i \lambda_p \quad (4)$$

where  $\Delta T/\Delta t$  is the rate of temperature change over a given period (K s<sup>-1</sup>),  $s$  is the volumetric heat capacity (J m<sup>-3</sup> K<sup>-1</sup>),  $\Delta x$  is the element height (m) and  $\lambda_p$  is the plan area fraction (%). And  $i$  represents the basic elements in urban volume, including building wall, roof, ground, street and indoor air, which is also denoted as internal building mass (iBLD). Based on this rate of 10-minute averaged temperature change,  $\Delta Q_S$  was calculated on 30-minute average. Table 5 provides detailed thermo-physical properties of the fundamental elements in the ideal urban volume for estimating  $\Delta Q_S$ .

### 2.4.3. Sky condition calculation

The classification of sky conditions, as outlined by Assunção et al. (2007) and Liu and Jordan (1960), involves the use of the clearness index  $K_t$ . This index serves as a quantitative measure to distinguish observation days based on varying levels of cloudiness. Specifically, a cloudy sky is associated with  $0 < K_t < 0.3$ , a partially cloudy sky with  $0.3 \leq K_t \leq 0.65$ , and a clear sky with  $0.65 < K_t < 1$ .

The instantaneous  $K_t$  is defined as the ratio of terrestrial to extra-terrestrial solar radiation, following the definition provided by Djafar et al. (2017):

$$K_t = G/G_0 \quad (5)$$

where  $G$  is the terrestrial global radiation on a horizontal surface and  $G_0$  is the extra-terrestrial solar radiation at the top of the atmosphere.  $G_0$  can be calculated as follows (Duffie & Beckman, 2013):

$$G_0 = I_{sc} \times \left[ 1 + 0.033 \cos\left(\frac{360N}{365}\right) \right] \times [\cos(\phi)\cos(\delta)\cos(\omega) + \sin(\phi)\sin(\delta)] \quad (6)$$

where  $I_{sc}$  is the solar constant and equals 1367 W m<sup>-2</sup>,  $N$  is the day number in the year,  $\phi$  is the latitude of the location in degrees, and  $\delta$  is the solar declination angle, which can be calculated as follows:

$$\delta = 23.45 \sin\left[\frac{360}{365} + (N + 284)\right] \quad (7)$$

$\omega$  is the sunrise/sunset hour angle in degrees, and the sunrise hour angle is the negative sunset hour angle, which can be defined as follows:

$$\omega = \cos^{-1}(-\tan\phi\tan\delta) \quad (8)$$

### 2.4.4. Temperature calculation

Temperature data are compared on specific days to study the diurnal variation. The spatially and temporally averaged temperatures are represented by  $\langle T \rangle$  and  $T'$  respectively, while  $T$  means the original temperature data. The temperature data were recorded continuously by an Agilent 34972A data logger at 3-second intervals and would be used as 10-minute averages of the measured temperature data to better represent the trend. Furthermore, we represented the spatial information of temperature using the subscript of  $T$ , for example,  $T_{rooftop}$ ,  $T_{wall}$ ,  $T_{air}$

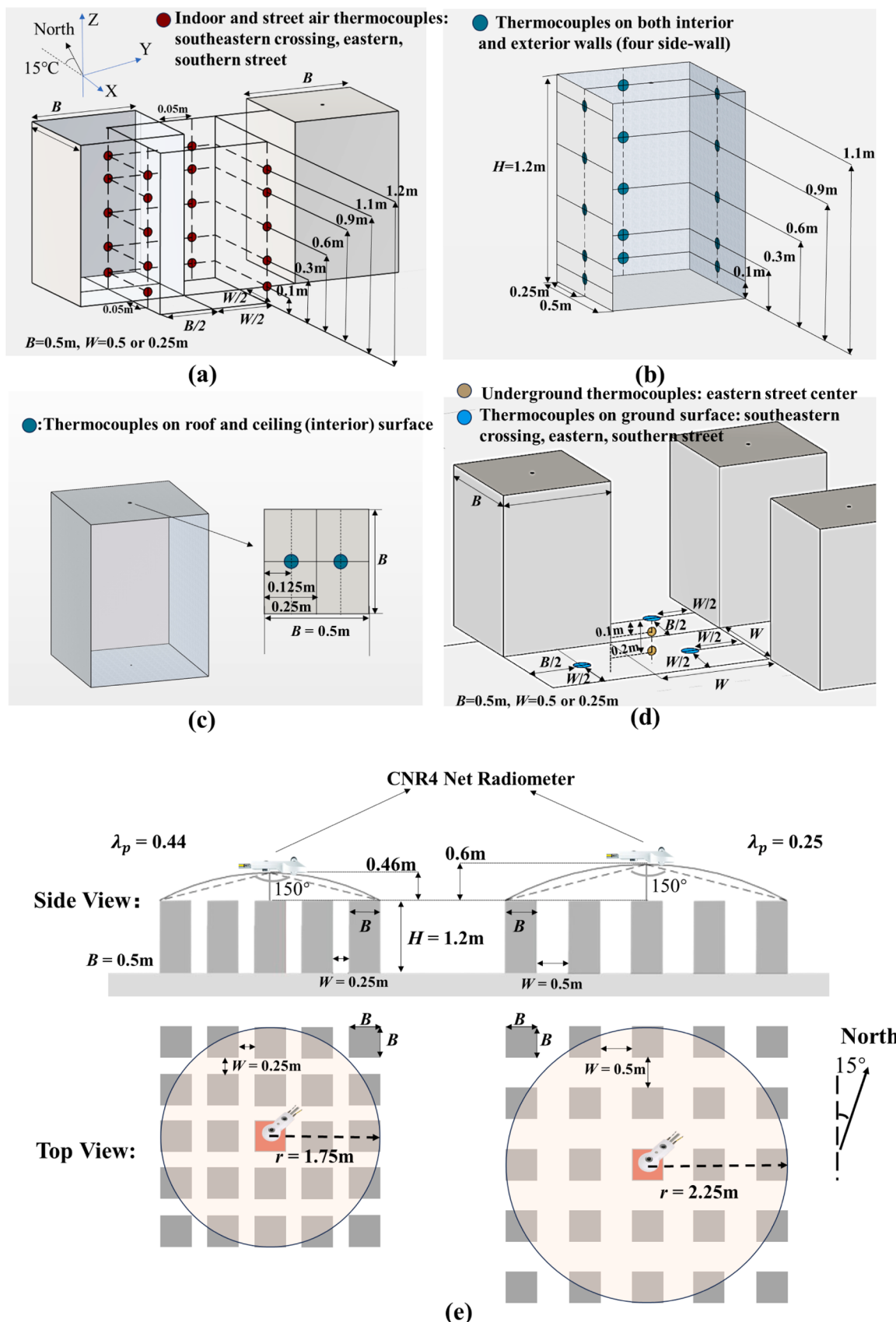


**Fig. 3.** Schematic of thermocouples placed in (a) indoor and street air, (b) wall surface, (c) roof and ceiling surface, (d) ground and underground. (e) side and top views of positions of CNR4 Net Radiometer as  $\lambda_p = 0.25, 0.44$ .

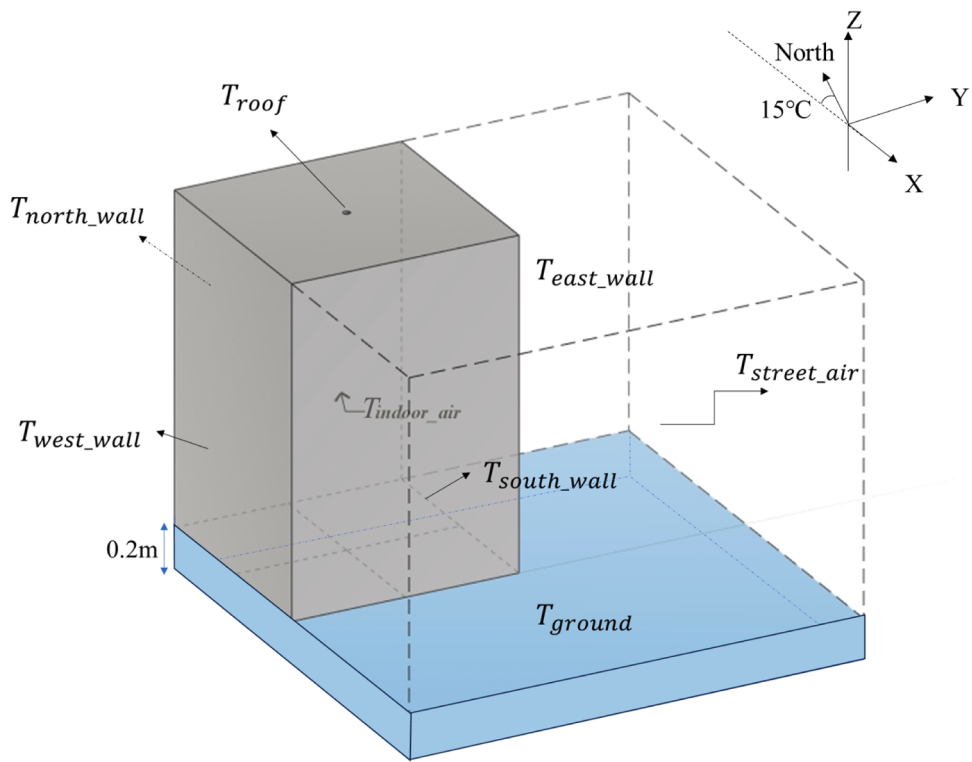


**Fig. 4.** Schematic illustration of a basic unit in 3D building clusters, including roof, wall, indoor and street air and ground.

**Table 5**

Summary of the thermophysical properties of the fundamental elements in the ideal 3D urban configuration at  $\lambda_p = 0.25, 0.44$ .

Basic element	Material	Volumetric heat capacity, $S$ ( $J m^{-3} K^{-1}$ )	Element height, $\Delta x$ (m)	Plan area fraction, $\lambda_{pi}$ ( $\lambda_p = 0.44$ )	Plan area fraction, $\lambda_{pi}$ ( $\lambda_p = 0.25$ )
Roof Wall (East, west, north and south wall)	Concrete	$1.496 \times 10^6$ $1.496 \times 10^6$	0.015 1.2	0.44 0.0133	0.25 0.0075
Ground		$1.496 \times 10^6$	0.2	0.56	0.75
Indoor air (iBLD)	Air	$1.211 \times 10^3$	1.17	0.3927	0.2209
Street air		$1.211 \times 10^3$	1.2	0.56	0.75

are the roof, wall, air temperature and specifically,  $T_{east\_wall}$ ,  $T_{west\_wall}$ ,  $T_{north\_wall}$  and  $T_{south\_wall}$  are the temperature of east, west, north and south wall,  $T_{indoor\_air}$  and  $T_{street\_air}$  are the temperature of indoor and street air. Throughout the experiment, all temperatures were consistently monitored except on June 22, where the temperature data at 0.3 m on the south wall were unavailable due to thermocouple failure.

#### 2.4.5. Albedo ( $\alpha$ ) calculation

The term “Albedo” is utilised to illustrate integrated and diffused hemispherical specular reflection of radiation across wavelengths ranging from 290 nm to 2500 nm (short wave) (Prado & Ferreira, 2005). According to Pearlmuter et al. (2007), the instantaneous albedo was calculated using Eq. (9):

$$\alpha_s = K \uparrow / K \downarrow \quad (9)$$

where  $K \downarrow$  is incoming shortwave radiation and  $K \uparrow$  is outgoing shortwave

radiation ( $W m^{-2}$ ).

Moreover, the average albedo ( $\alpha_a$ ) for a given timeframe was determined as the ratio of reflected radiation to incident solar radiation, both integrated across the hemisphere and throughout the day, which was estimated by Eq. (10) (Aida, 1982; Morini et al., 2017; Taha et al., 1992):

$$\alpha_a = \frac{\int_{t_0}^{t_1} K \uparrow(t) dt}{\int_{t_0}^{t_1} K \downarrow(t) dt} \quad (10)$$

where  $t_0$  and  $t_1$  represent the start and end time, respectively.

## 3. Results and discussion

### 3.1. Impact of coating mode on low- and medium-density urban canopy

#### 3.1.1. Albedo

Fig. 5a-c display the daily variation of albedo ( $\alpha_s$ ) and downward shortwave radiation under different coating modes and building area densities, with a similar clear sky index ( $K_t \sim 0.5$ ). For uncoated cases, the daytime (6:00–18:00) average albedo ( $\alpha_a$ ) for low-density ( $\lambda_p = 0.25$ ,  $H/W = 2.4$ ) ranged from 0.13 to 0.14, while for medium-density ( $\lambda_p = 0.44$ ,  $H/W = 4.8$ ) urban canopies, it varied from 0.16 to 0.17. Among the coating modes, RW-type induced the most significant changes in reflectance, increasing the overall average albedo by 121.4 % and 125.0 % at  $\lambda_p = 0.25$  and 0.44, respectively. The W-type had the least impact on overall albedo. As noted by Lu et al. (2023), its impact on the albedo of the medium-density canopy ( $\lambda_p = 0.44$ ) was minimal, largely due to the sidewalls’ limited sky view factor. For both coated groups, the overall albedo remained nearly unchanged across the two different densities ( $\alpha_a \sim 0.2$ ). However, the increase in  $\alpha_a$  after applying coatings for low-density building clusters reached 42.9 %, significantly higher than the observed effect at medium-density (17.6 %). Conversely, for R-type, roof coating resulted in an 84.6 % increase in  $\alpha_a$  for low-density building clusters, compared to a substantial 100.0 % increase for medium-density clusters. Moreover, aside from W-type cases, we

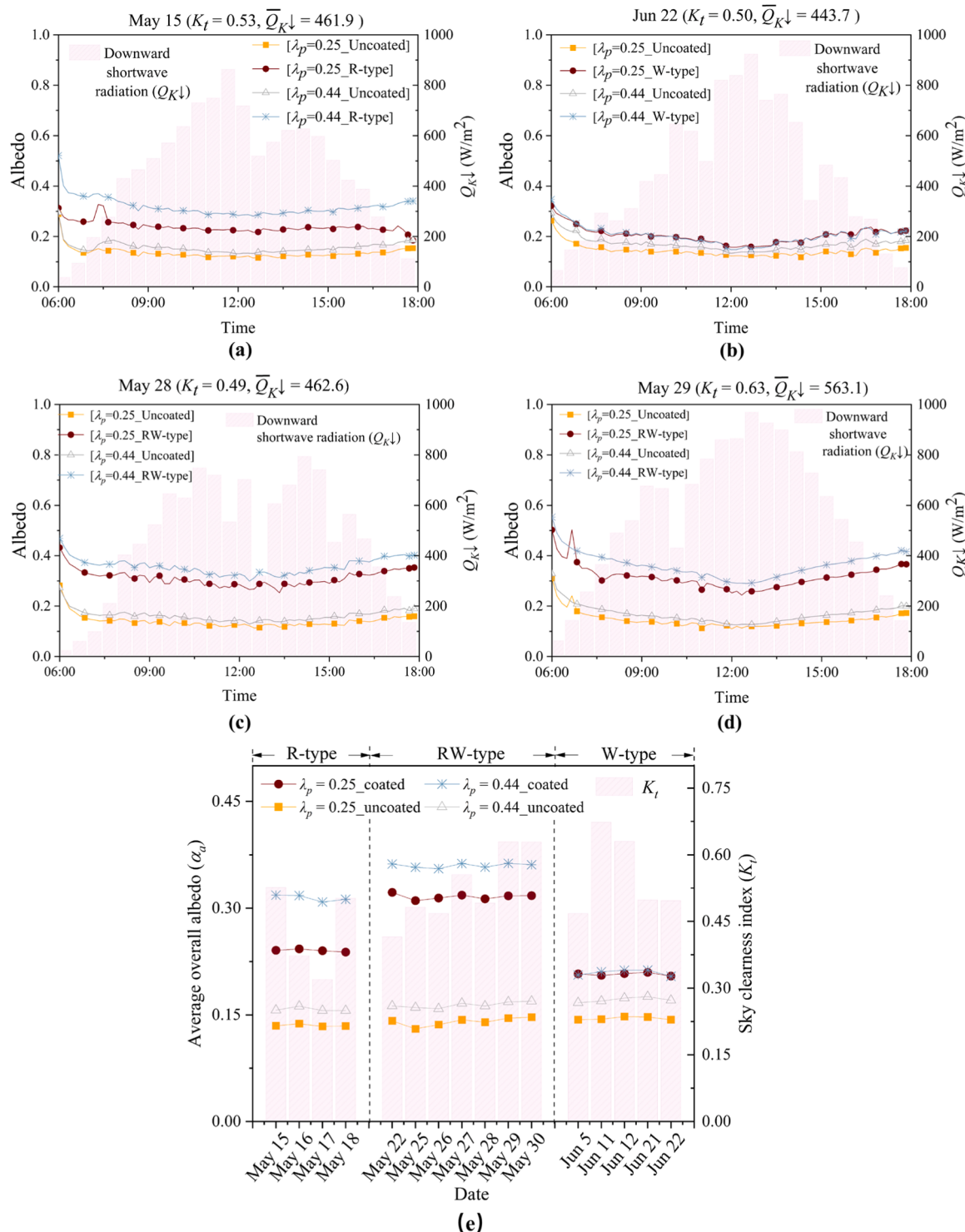


**Fig. 5.** Diurnal variations of overall urban albedo ( $\alpha_a$ ) and downward shortwave radiation ( $Q_{K\downarrow}$ ) for various cases with  $\lambda_p = 0.25, 0.44$  ( $Q_{K\downarrow}$  is averaged  $Q_{K\downarrow}$  during 6:00–18:00), sky conditions, and three coating modes on four selected days: (a) R-type, (b) W-type, (c)-(d) RW-type, and (e) average overall albedo ( $\alpha_a$ ) and sky clearness index ( $K_t$ ) during non-rainy days.

observed that the albedo ( $\alpha_a$ ) in R-type, RW-type, and uncoated scenarios at medium-density building clusters was consistently higher than in low-density settings, with an increase ranging from 0.02 to 0.03 for uncoated and 0.04 to 0.08 for coated cases.

To compare the impact of  $K_t$  on overall albedo under different building area densities and coating types, we list the average overall albedo ( $\alpha_a$ ) and sky clearness index ( $K_t$ ) of all the non-rainy days (Fig. 5e). We found that when  $K_t$  ranged from 0.32 to 0.53 (R-type) and

from 0.47 to 0.67 (W-type),  $|\Delta\alpha_a|$  was  $<0.01$  under the same coating type and building area density; for RW-type cases, when  $K_t$  ranged from 0.41 to 0.63,  $|\Delta\alpha_a|$  was also  $<0.01$ , except the uncoated cases at  $\lambda_p = 0.25$  (the variation of  $\alpha_a$  was  $\sim 0.02$ ). Additionally, we selected two days (May 28, 29) under RW-type with average downward shortwave radiation during the day (6:00–18:00) ( $Q_{K\downarrow}$ ) of 462.6 and 563.1 W m<sup>-2</sup>, respectively. The differences of  $\alpha_a$  were also very small ( $<0.01$ , Fig. 5c, d). Therefore, under non-rainy conditions, the overall albedo for TR-W

cases is essentially unaffected by the degree of sky clearness and downward shortwave radiation.

### 3.1.2. Surface temperature difference at roof and building walls

**Fig. 6** illustrates the average cooling of different surfaces, including roofs, ceilings, and all four sidewalls during the daytime (6:00–18:00). Surprisingly, for the wall temperature  $T_{wall}$  (**Fig. 6a-d**), we discovered that the average cooling magnitude and maximum cooling (**Table 6**) produced by R-type and W-type in medium-density building clusters were close. Despite the coating was directly applied to the wall surface, the average cooling of four walls under W-type was even less than that of R-type, ranging from 0.2 to 0.4 °C. The proportion of surface (wall, roof, and ceiling) cooling time ( $\leq -1$  °C) under W-type during the daytime (6:00–18:00) was only 0.0–31.3 % at  $\lambda_p = 0.44$ . However, for low-density buildings ( $\lambda_p = 0.25$ ), we found that W-type significantly enhanced the cooling effect on building sidewalls. The average cooling ranged from 2.3 to 2.7 °C, increasing nearly 3–4 times, with the proportion of wall surface cooling time ( $\leq -2$  °C) reaching 56.7–82.5 %. Similar effects were also observed with RW-type coatings, where under similar weather conditions, the average wall cooling reached 1.1–1.6 °C at  $\lambda_p = 0.44$ , while at  $\lambda_p = 0.25$ , this value increased to 3.8–4.4 °C. Moreover, under clearer weather conditions ( $K_t = 0.63$ ), the average sidewall cooling increased by 0.3 °C for  $\lambda_p = 0.44$  and by 0.2–0.5 °C for  $\lambda_p = 0.25$ . The cooling effect of W-type on building sidewalls is highly dependent on the sky view factor. In low-density buildings, a larger sky view factor determines the amount of direct solar radiation received by the wall surface. When using high-reflectance coatings to significantly increase the wall's albedo, it leads to stronger reflected radiation, resulting in a more substantial cooling effect.

Both R-type and RW-type coatings significantly reduce the roof and ceiling surface temperatures. Under similar weather conditions at  $\lambda_p = 0.44$  ( $K_t \sim 0.5$ ), two coating modes exhibited comparable average cooling effects. Specifically, the roof temperatures decreased by 8.0 °C and 7.5 °C for R-type and RW-type, respectively, while the ceiling temperatures decreased by 7.5 °C and 6.9 °C. In low-density buildings ( $\lambda_p = 0.25$ ), both the roof and ceiling experience notably higher cooling magnitudes, particularly with RW-type coatings, which increase by 2.1 °C and 2.2 °C for the roof and ceiling, respectively. Regarding the proportion of cooling time during the daytime (6:00–18:00), the use of roof coatings (R-type, RW-type) enables the roof and ceiling to experience cooling exceeding 2 °C for 82.2–86.8 %. For RW-type, we found that under clearer weather conditions ( $K_t = 0.63$ ), the cooling effects became more pronounced, with an average temperature difference between the roof and ceiling increasing by 1.1–1.3 °C at  $\lambda_p = 0.25$ , and by 0.8–0.9 °C at  $\lambda_p = 0.44$ . Moreover, the proportion of cooling time ( $\leq -2$  °C) for the roof and ceiling surface during daytime (6:00–18:00) reached 89–91.5 %. Besides, although the cooling effect of W-type on the roof was relatively small at  $\lambda_p = 0.44$ , it was evident that W-type can reduce the roof surface temperature, and it was also influenced by building area density: the cooling amplitude under low building area density ( $\lambda_p = 0.25$ ) was higher. The  $\langle \Delta T_{roof,max} \rangle$  reached  $-6.0$  °C, approximately 2.1 °C lower than that at  $\lambda_p = 0.44$ .

### 3.1.3. Temperature difference of indoor and street air

The application of cooling coatings results in significant reductions in daytime indoor air temperatures, particularly with RW-type. **Fig. 7a-f** illustrates the diurnal variation of indoor air temperature differences under three coating modes at  $\lambda_p = 0.25$  and 0.44 ( $K_t \sim 0.5$ ). Notably, building area density plays a crucial role in the indoor cooling effect in cases with wall coatings (W-type and RW-type). At  $\lambda_p = 0.25$ , the W-type and RW-type cases showed an average indoor air cooling of 2.3 °C and 3.8 °C. However, this cooling dropped to only 0.7 °C and 1.6 °C, respectively, as  $\lambda_p$  increased to 0.44. The R-type's cooling effect showed minimal sensitivity to changes in building area density, consistently achieving an overall indoor temperature reduction of about 1.2 °C. This effect was most pronounced in the upper layers ( $z = 1.1, 0.9$  m),

reaching an average cooling of 2.0 °C, and decreasing with lower heights.

Among these coating modes, the minimal cooling effect was observed at the bottom layers ( $z = 0.3, 0.1$  m). At the upper layers ( $z = 1.1, 0.9$  m), RW-type coatings achieved the highest indoor air cooling, with reductions reaching up to  $-8.1$  °C. The average cooling effects at  $\lambda_p = 0.25$  and  $\lambda_p = 0.44$  were 5.1 °C and 3.1 °C, respectively. This was followed by W-type coatings, which produced cooling effects of 2.6 °C and 1.2 °C, and R-type coatings, which resulted in 1.9 °C and 2.0 °C, respectively. The temperature difference between the middle and upper levels was minimal for W-type, only 0.3 °C, whereas for RW-type and R-type, the differences were notably larger, at 1.3–1.7 °C and 0.8–0.9 °C, respectively.

For lower levels ( $z = 0.3, 0.1$  m), the cooling gain from the wall coatings was closely linked to building area density, with more significant vertical differences in high-density settings. At  $\lambda_p = 0.25$ , RW-type, W-type, and R-type coatings led to average temperature reductions of 2.5, 1.9, and 0.8 °C, respectively, with the maximum reductions reaching 4.3, 2.9, and 1.1 °C. However, at  $\lambda_p = 0.44$ , the average reductions for the three coating modes were only 0.2, 0.1, and 0.4 °C, with maximum reductions between 0.5 to 0.6 °C. This phenomenon may be attributed to reduced direct solar radiation access to lower surfaces within medium-density building clusters. Consequently, reflected radiation becomes a primary source, amplified by high-reflectance walls, potentially leading to increased radiation absorption and higher temperatures indoors and at lower wall surfaces. In addition, we found that under clearer weather conditions ( $K_t = 0.63$ ), as depicted in **Fig. 7g-h**, the average indoor air cooling induced by RW-type increased by approximately 0.3–0.4 °C across upper, medium, and bottom levels.

Besides, we noted a correlation between cooling peaks induced by wall coatings and solar altitude angles. In the morning, direct sunlight illuminated east walls, enabling reflective surfaces to reduce absorbed radiation and lower indoor temperatures. As solar altitude angles increased, incident radiation angles also rose gradually, reducing radiation perpendicular to the wall surface. This led to a decrease in reflected radiation and, consequently, reduced cooling of both the wall surface and indoor air. Hence, the first cooling peak occurred in the morning, with a similar trend observed in the afternoon due to high-reflectance west walls. Both W-type and RW-type constructions exhibited dual cooling peaks, typically around 10:00 and 16:00, and 11:00 and 15:00, respectively. For the R-type, the cooling peak occurred around 11:00–12:00, earlier in low-density buildings ( $\lambda_p = 0.25$ ).

In our study on street canyon air temperature, we found results that align with those reported by Lu et al. (2023). **Fig. S1a-f** displays the diurnal variation of street air temperature at  $z = 1.1, 0.9, 0.6, 0.3, 0.1$  m and the street air temperature differences under three coating modes at  $\lambda_p = 0.25$  and 0.44 ( $K_t \sim 0.5$ ). The street air temperature variations for both the coated and uncoated groups were largely comparable, with the overall temperature differences falling within the margin of error for the thermocouples (**Table 4**). As a result, it remains challenging to ascertain whether the coating had a measurable cooling effect on the street air. However, at  $\lambda_p = 0.25$ , the average temperature difference  $\langle \Delta T_{street,air} \rangle$  (6:00–18:00) for the W-type and RW-type cases was 0.6–0.8 °C lower than at  $\lambda_p = 0.44$ . This is consistent with the results of wall surface cooling, indicating that cool wall coatings may have a more pronounced cooling effect both indoors and outdoors in areas with lower building area density.

### 3.1.4. Heat storage flux ( $\Delta Q_s$ )

**Fig. 8** illustrates the diurnal variation of the heat storage flux ( $\Delta Q_s$ , calculated by ESTM) and the net solar radiation ( $Q^*$ ) of coated and uncoated cases at  $\lambda_p = 0.25$  and 0.44. We observed a strong correlation between the variations in heat storage flux and net radiation. For instance, a sharp decrease in net radiation led to a corresponding reduction in building heat storage flux. Buildings generally started to absorb heat at 6:00, with heat storage flux increasing alongside the

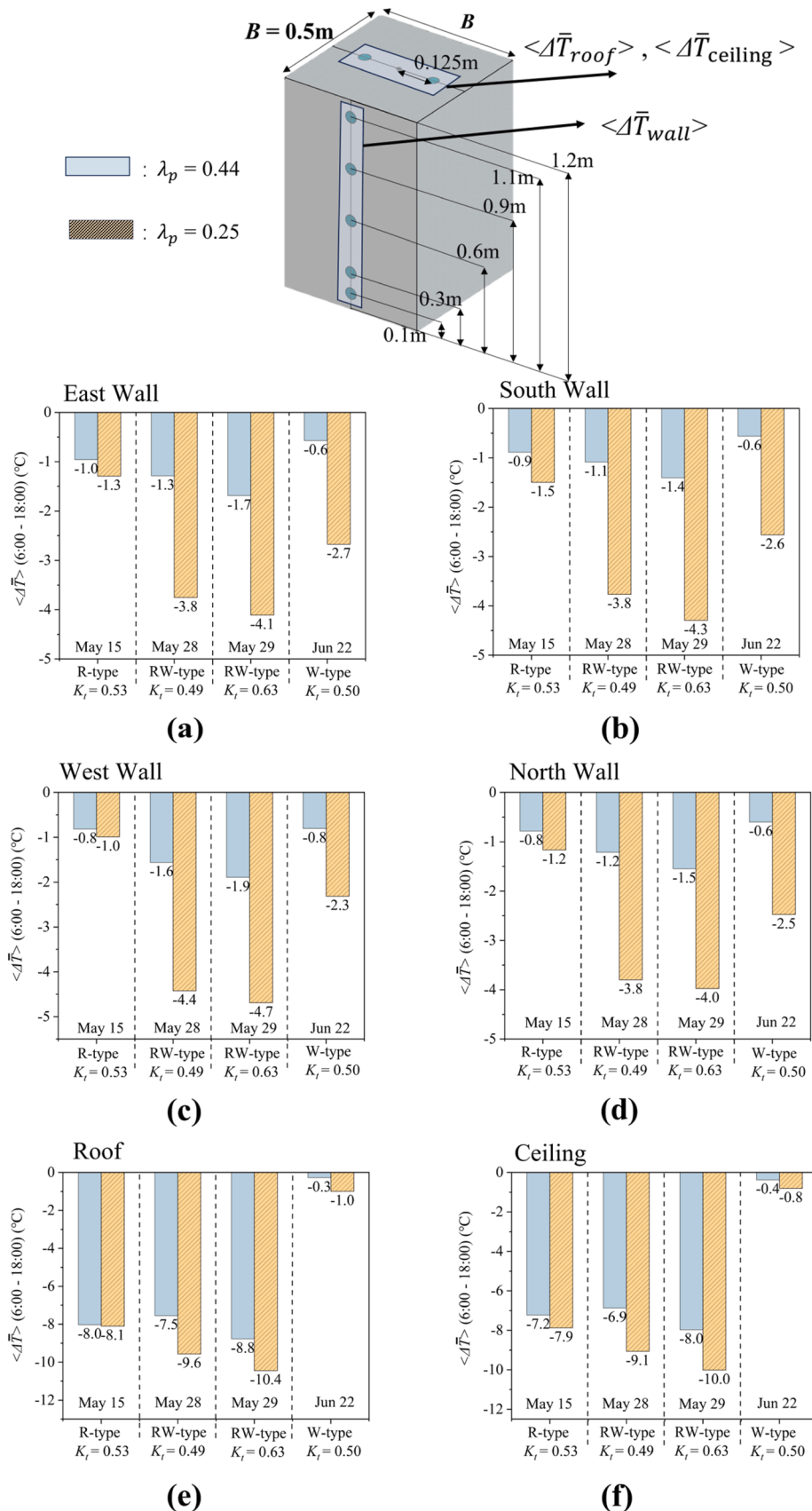


**Fig. 6.** Bar charts of  $\langle \Delta T_{wall} \rangle$ ,  $\langle \Delta T_{roof} \rangle$  and  $\langle \Delta T_{ceiling} \rangle$  from 6:00 to 18:00 between TR-W coating and uncoated cases with different building area densities ( $\lambda_p = 0.25, 0.44$ ), sky conditions ( $K_t \sim 0.5$  and  $0.6$ ), and three coating modes (R-type, W-type, RW-type) on four selected days (May 15, 28, 29, Jun 22): (a) East wall, (b) South wall, (c) West wall, (d) North wall, (e) Roof, (f) Ceiling.

**Table 6**

Summary of the maximum coated building surface (wall, roof and ceiling) cooling ( $\langle \Delta T_{max} \rangle$ ) during the daytime (6:00–18:00) for various cases with different building area densities, sky conditions and coating modes.

Date	Case name	Variables	Maximum cooling ( $\langle \Delta T_{max} \rangle$ ) (°C)					
			$\langle \Delta T \rangle = \langle T_{coated} \rangle - \langle T_{uncated} \rangle$					
			East wall	South wall	West wall	North wall	Roof	Ceiling
May 15 ( $K_t=0.53$ )	[ $\lambda_p=0.44$ _R-type]	Building area density, R-type	-1.4	-1.4	-1.6	-1.3	-13.6	-12.3
	[ $\lambda_p=0.25$ _R-type]		-2.2	-2.6	-1.7	-1.7	-15.3	-13.6
Jun 22 ( $K_t=0.50$ )	[ $\lambda_p=0.44$ _W-type]	Building area density, W-type	-1.3	-1.0	-2.3	-1.7	-3.9	-1.7
	[ $\lambda_p=0.25$ _W-type]		-5.0	-3.6	-5.4	-4.4	-6.0	-1.8
May 28 ( $K_t=0.49$ )	[ $\lambda_p=0.44$ _RW-type]	Building area density, RW-type	-2.3	-1.9	-3.3	-2.4	-13.7	-11.8
	[ $\lambda_p=0.25$ _RW-type]		-6.7	-6.1	-9.3	-6.6	-16.5	-15.2
May 29 ( $K_t=0.63$ )	[ $\lambda_p=0.44$ _RW-type]	Clearer sky condition, building area density, RW-type	-2.8	-2.1	-3.5	-2.8	-14.9	-13.7
	[ $\lambda_p=0.25$ _RW-type]		-7.1	-6.5	-8.7	-6.1	-17.4	-15.4

downward shortwave radiation. After the solar elevation peaked, a sharp decrease was observed, then a gradual rise below zero. This pattern, most notably illustrated in Fig. 8d, without significant fluctuations in net radiation during the period. According to Fig. S2, this pattern primarily results from the impact of ground heat storage flux density, which varied significantly due to the building's east-side shading. In clearer weather, ground heat storage flux density had a more significant impact on total heat storage flux, causing more noticeable variations. A simplified diagram (Fig. 8e) was included to aid in understanding the discussed fluctuations in building heat storage flux. Hence, under clear sky conditions, areas with lower building area density experience an earlier peak and a later minimum in ground heat storage flux density.

Besides, low-density building clusters ( $\lambda_p = 0.25$ ) exhibited higher heat storage flux compared to medium-density ones ( $\lambda_p = 0.44$ ) (Table 7). For uncoated cases ( $K_t \sim 0.5$ ), the averaged heat storage fluxes in low-density building clusters were  $6.3\text{--}11.0\text{ W m}^{-2}$  higher than in medium-density. In clearer weather ( $K_t = 0.63$ ), the disparity became more pronounced, with the heat storage flux in low-density building clusters reaching up to  $538.6\text{ W m}^{-2}$  for the uncoated case—approximately double that observed in medium-density clusters. The daily averaged heat storage flux difference between medium and low-density clusters also increased, from  $6.3\text{ W m}^{-2}$  to  $8.5\text{ W m}^{-2}$ . Moreover, we observed that in low-density clusters ( $\lambda_p = 0.25$ ), the average ground heat storage flux densities were at least double those in medium-density clusters ( $\lambda_p = 0.44$ ) under similar conditions. This phenomenon may be attributed to the increased direct sunlight received and absorbed by the ground over extended periods at  $\lambda_p = 0.25$ .

As shown in Table 7, high-reflectance coatings can slightly reduce building heat storage flux. Generally, applying coatings decreased the averaged heat storage flux in buildings, mainly affecting the heat storage flux densities of building surfaces like roofs and sidewalls. For R-type, the reduction in heat storage flux density on roofs was notable at  $\lambda_p = 0.44$ , showing a decrease of  $0.6\text{ W m}^{-2}$ , three times the reduction observed at  $\lambda_p = 0.25$ . Furthermore, roof coatings significantly reduce the heat storage flux density on sidewalls by an average of  $0.3\text{--}0.6\text{ W m}^{-2}$  at  $\lambda_p = 0.44$ . However, for  $\lambda_p = 0.25$ , the impact on sidewall heat storage flux density is negligible. For W-type and RW-type, both density scenarios exhibited comparable reductions in wall heat storage flux density, ranging from  $0.1$  to  $0.3$  and  $0.5\text{--}0.8\text{ W m}^{-2}$ , respectively, and in roof heat storage flux density, ranging from  $0$  to  $0.1$  and  $0.5\text{--}0.7\text{ W m}^{-2}$ . Under clearer weather conditions, these reductions (RW-type) varied by  $<0.1\text{ W m}^{-2}$ .

### 3.2. Impact of coating mode and coating material on medium-density urban canopy

Research on near-infrared reflective coatings (NIR coatings) in real or scaled urban environments is limited, which might complicate the simulation validation. This subsection examines the effects of two traditional high-reflectance coatings (TR-W, TR-Y) and a modified yellow coating with 30 % NIR powder on medium-density building clusters ( $\lambda_p = 0.44$ ). We applied these coatings under two coating modes to four building clusters to quantitate their effects on albedo, surface cooling, indoor air temperature, and heat storage flux. We specifically analysed data from July 6 and July 12 to provide a detailed parameterized assessment.

#### 3.2.1. Albedo

The NIR-Y coatings applied to buildings exhibit consistently higher albedo throughout the day than TR-W and TR-Y coatings. Fig. 9 illustrates the diurnal variation in overall albedo ( $\alpha_s$ ) for two coating patterns under the W-type and RW-type. We observed that the NIR-Y coating significantly enhanced the overall albedo of the building cluster. Compared to uncoated cases with the overall albedo of 0.18, TR-Y and NIR-Y coatings increase the average albedo ( $\alpha_a$ ) by 42.9 % and 53.5 % for W-type, respectively, while the percentage only 16.0 % for white coating. For RW-type, TR-Y and NIR-Y coatings achieve  $\alpha_a$  values of 0.43 and 0.47, surpassing the 0.36 of white coatings. In addition, we observed that during Period II, when  $K_t$  ranged from 0.37 to 0.63 (non-rainy days),  $|\Delta\alpha_a|$  was  $<0.01$  for most cases under the same coating type and material except for the NIR-Y and TR-Y cases under RW-type, the variation of  $\alpha_a$  was about 0.02. This implies that building clusters coated with NIR-Y coatings absorb less solar radiation, thereby enhancing the mitigation of urban heat environments. Similar to TR coatings, the overall albedo for NIR coatings on non-rainy days is also largely unaffected by the degree of sky clearness and downward shortwave radiation.

#### 3.2.2. Surface temperature difference at roof and building walls

Fig. 10 presents the daytime (6:00–18:00)  $\langle \Delta T_{wall} \rangle$ ,  $\langle \Delta T_{roof} \rangle$  and  $\langle \Delta T_{ceiling} \rangle$  under TR-W, TR-Y and NIR-Y coatings for both W-type and RW-type at  $\lambda_p = 0.44$ . Although the TR-Y coating had higher albedo and reflectance, it was less effective at cooling the four walls, averaging a temperature reduction of only  $0.4\text{--}1.2\text{ }^\circ\text{C}$ ,  $0.2\text{--}0.5\text{ }^\circ\text{C}$  lower than the TR-W coating. In contrast, the NIR-Y coating markedly increased  $\langle \Delta T_{wall} \rangle$  by 2–3 times compared to the TR-Y coating, leading to maximum temperature reductions of  $3.0\text{ }^\circ\text{C}$  in W-type and  $4.1\text{ }^\circ\text{C}$  in RW-type, as detailed in Table 8. Additionally, the cooling efficiency of different

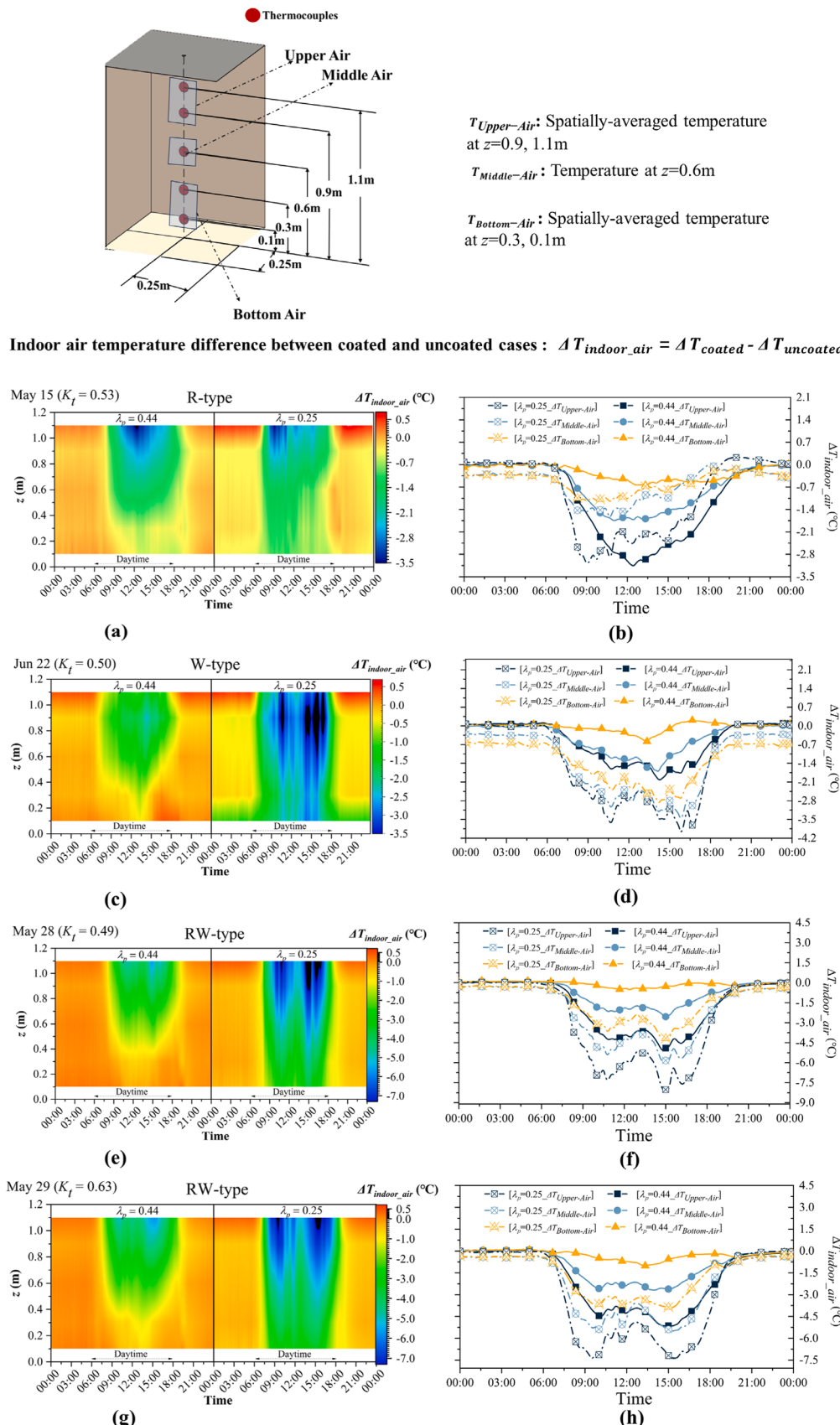


**Fig. 7.** Heatmap of indoor air temperature difference  $\Delta T_{\text{indoor\_air}}$  at different heights ( $z = 1.1, 0.9, 0.6, 0.3 and  $0.1$  m) between TR-W coating and uncoated cases and the corresponding diurnal variations of  $\langle \Delta T_{\text{indoor\_air}} \rangle$  across three levels (Upper-, Middle- and Bottom-air) with different building area densities ( $\lambda_p = 0.25, 0.44$ ), sky conditions, and three coating modes on four selected days (May 15, 28, 29, Jun 22): (a)-(b) R-type,  $K_t=0.53$ , (c)-(d) W-type,  $K_t=0.50$ , (e)-(f) RW-type,  $K_t=0.49$ , (g)-(h) RW-type,  $K_t=0.63$ .$

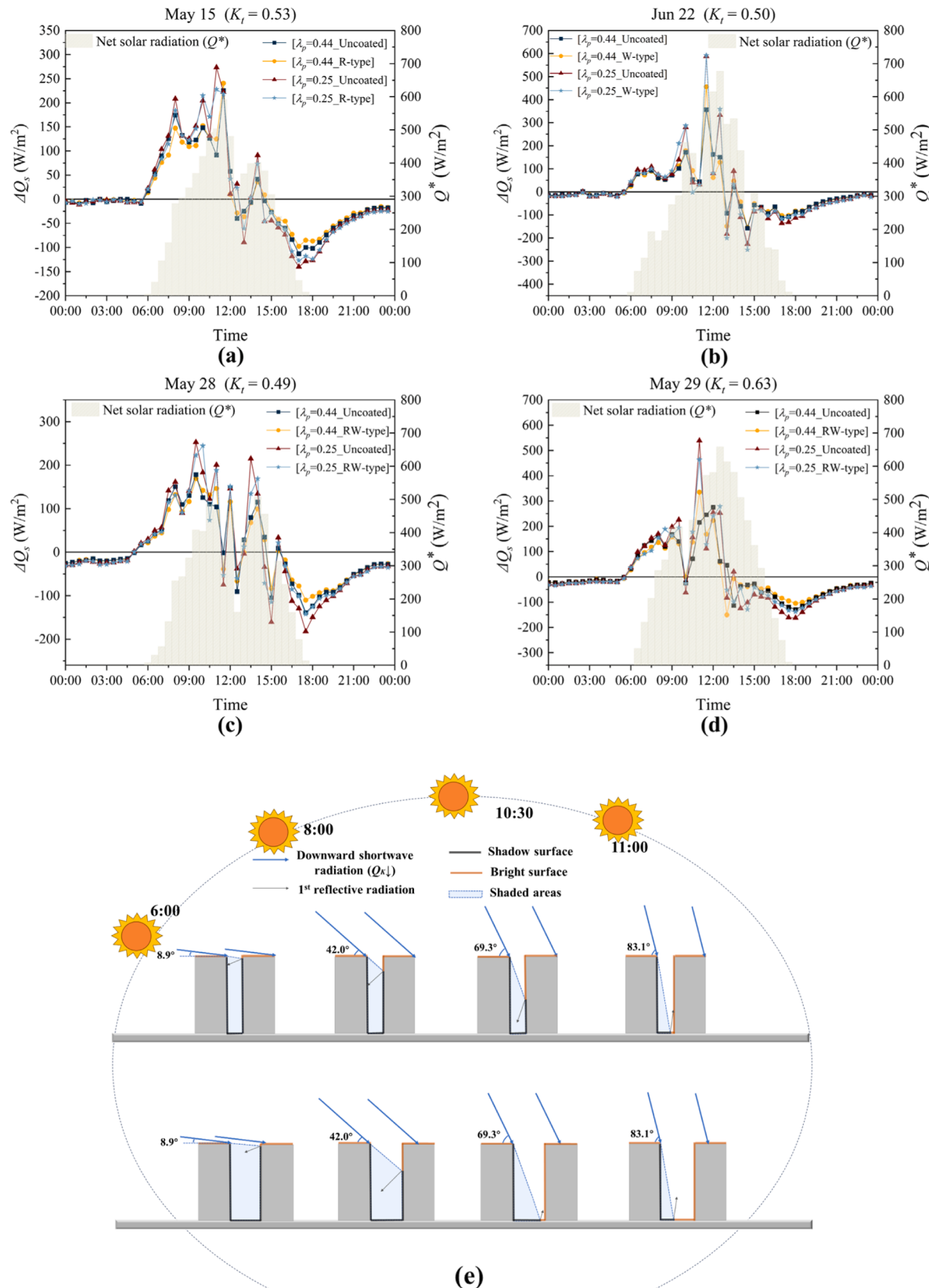


**Fig. 8.** Diurnal variations of the coated and uncoated building heat storage flux  $\Delta Q_s$  (calculated by the ESTM) and the net solar radiation  $Q^*$  for various cases with different building area densities ( $\lambda_p = 0.25, 0.44$ ), sky conditions, and three coating modes on four selected days (May 15, 28, 29, Jun 22): (a) R-type,  $K_t = 0.53$ , (b) W-type,  $K_t = 0.50$ , (c) RW-type,  $K_t = 0.49$ , (d) RW-type,  $K_t = 0.63$ , (e) Schematic of the incoming radiation at different times.

**Table 7**

Summary of averaged and maximum energy flux of  $Q^*$ ,  $\Delta Q_S$  (calculated by ESTM), and averaged heat storage flux density during daytime (6:00–18:00) for various cases with different building area densities, sky conditions and coating modes.

Date	Case name	$\Delta Q_{S,\max}$ (W m <sup>-2</sup> )	$\Delta Q_{S,\text{avg}}$ (W m <sup>-2</sup> )	$Q^*_{\max}$ (W m <sup>-2</sup> )	$Q^*_{\text{avg}}$ (W m <sup>-2</sup> )	Averaged heat storage flux density (W m <sup>-2</sup> ) (6:00–18:00)							
						East wall	South wall	West wall	North wall	Roof	Ground	Indoor air	Street air
May 15, ( $K_t=0.53$ )	[ $\lambda_p = 0.44$ _R-type]	240.7	40.5	591.5	286.3	5.8	5.7	6.1	6.0	2.9	13.7	0.1	0.2
	[ $\lambda_p = 0.44$ _Uncoated]	225.6	42.4			6.2	6.2	6.4	6.6	3.5	13.3	0.1	0.2
	[ $\lambda_p = 0.25$ _R-type]	228.2	51.0			3.9	3.9	4.4	4.2	1.8	32.4	0.1	0.2
	[ $\lambda_p = 0.25$ _Uncoated]	273.4	50.3			3.9	3.8	4.2	4.1	2.0	31.9	0.1	0.2
Jun 22, ( $K_t=0.50$ )	[ $\lambda_p = 0.44$ _W-type]	455.8	31.0	676.7	281.3	3.7	3.7	3.8	3.8	2.0	13.8	0.1	0.1
	[ $\lambda_p = 0.44$ _Uncoated]	356.6	30.1			3.9	3.8	4.0	4.1	2.1	12.1	0.1	0.1
	[ $\lambda_p = 0.25$ _W-type]	592.2	41.9			2.3	2.3	2.4	2.4	1.3	31.2	0.1	0.1
	[ $\lambda_p = 0.25$ _Uncoated]	588.1	41.1			2.4	2.4	2.6	2.6	1.3	29.6	0.1	0.1
May 28, ( $K_t=0.49$ )	[ $\lambda_p = 0.44$ _RW-type]	169.5	41.2	507.2	275.5	5.7	5.6	5.9	5.9	2.7	15.1	0.1	0.1
	[ $\lambda_p = 0.44$ _Uncoated]	178.4	42.9			6.2	6.2	6.6	6.7	3.4	13.5	0.1	0.1
	[ $\lambda_p = 0.25$ _RW-type]	244.6	47.8			3.3	3.3	3.7	3.5	1.5	32.1	0.1	0.2
	[ $\lambda_p = 0.25$ _Uncoated]	252.7	49.2			3.8	3.8	4.5	4.3	2.0	30.5	0.1	0.2
May 29, ( $K_t=0.63$ )	[ $\lambda_p = 0.44$ _RW-type]	335.3	49.1	658.2	336.3	6.4	6.4	6.6	6.6	3.2	19.5	0.2	0.2
	[ $\lambda_p = 0.44$ _Uncoated]	275.0	51.5			7.0	7.0	7.4	7.5	3.9	18.2	0.2	0.2
	[ $\lambda_p = 0.25$ _RW-type]	463.7	59.1			3.9	3.9	4.2	4.1	1.8	40.9	0.1	0.2
	[ $\lambda_p = 0.25$ _Uncoated]	538.6	60.0			4.3	4.4	5.0	4.9	2.4	38.7	0.1	0.2

materials was also evident in the proportion of cooling time (Table S2). For instance, TR-W and TR-Y coatings rarely achieved wall cooling below 2 °C, while the proportion of cooling time ( $\leq -2$  °C) under the NIR-Y coating reached 8.2–27.1 % for the four walls.

Regarding roof and ceiling temperatures, we observed that all three coating materials under W-type decreased both roof and ceiling surface temperatures, although the reductions were minimal. For RW-type, the cooling effects of the TR-W and TR-Y coatings were similar, while in contrast, the NIR-Y coating achieved significantly higher average cooling on both the roof and ceiling by 2.2 °C and 1.7 °C than TR-W coating, respectively. As indicated in Table 8, it achieved maximum roof and ceiling cooling of 17.3 °C and 14.7 °C, nearly 3 °C more than the white and yellow coating.

### 3.2.3. Temperature difference of indoor air

Compared to the TR-W coating, both the TR-Y and NIR-Y coatings offer greater cooling benefits for indoor air. Fig. 11a-c displays at different heights ( $z = 1.1, 0.9, 0.6, 0.3$ , and 0.1 m) for coated and uncoated cases under W-type and RW-type at  $\lambda_p = 0.44$ . For W-type, the average indoor air cooling was 0.8 °C, 0.9 °C, and 1.4 °C for TR-W, TR-Y, and NIR-Y coatings. At upper level ( $z = 1.1, 0.9$  m), TR-Y and NIR-Y coatings decreased the by 1.9 °C and 2.4 °C, respectively, compared to only 1.2 °C for the TR-W coating. At the middle level ( $z = 0.6$  m), the TR-Y and NIR-Y coatings offered an additional cooling of 0.2 °C and 0.8 °C over the 1.0 °C averaged cooling provided by the TR-W coating. However, at lower levels ( $z = 0.3, 0.1$  m), both coatings exhibited a noticeable warming effect, particularly the TR-Y coating, which raised the lower air temperature by an average of 0.6 °C compared to the uncoated case.

For RW-type, the TR-W, TR-Y and NIR-Y coatings resulted in overall indoor cooling amplitudes of 1.7 °C, 1.8 °C, and 2.9 °C. The NIR-Y coating achieved an average cooling of 5 °C cooling at upper-level indoor air, surpassing the TR-W and TR-Y coatings by 1.9 °C and 1.3 °C, respectively, with a peak cooling of 6.7 °C. At middle-level, the NIR-Y,

TR-W and TR-Y coatings reduced the  $\Delta T_{\text{indoor air}}$  by 3.0 °C, 2.0 °C, and 1.7 °C, respectively. Notably, the NIR-Y coating significantly mitigated warming at the bottom level ( $z = 0.1$  m), achieving an average cooling of 0.7 °C, compared to the TR-Y coating, which only reduced its warming effect from 0.7 °C to 0.3 °C.

### 3.2.4. Heat storage flux ( $\Delta Q_S$ )

Fig. 12a-b illustrates the diurnal variation of building heat storage flux ( $\Delta Q_S$ , calculated by ESTM) and the net solar radiation  $Q^*$  for various cases at  $\lambda_p = 0.44$ . As discussed in Section 3.1.4, high-reflectance coatings do not significantly impact building heat storage flux. Fig. S3 and Table 9 show the diurnal variations of the heat storage flux densities and the averaged heat storage flux densities of roof, walls, ground and indoor and outdoor air during daytime (6:00–18:00). Clearly, NIR-Y coating under RW-type generally achieve lower averaged heat storage flux densities of walls and roof. For W-type, the effects across three coating modes were similar, resulting in the averaged heat storage flux densities of the four walls during daytime (6:00–18:00) being reduced by 0.1–0.6 W m<sup>-2</sup> compared to the uncoated case. For RW-type, the NIR-Y cases show the most substantial reduction in heat storage flux density for walls and roofs, ranging from 1.1 to 1.7 W m<sup>-2</sup> for walls and 1.2 W m<sup>-2</sup> for roofs, surpassing TR-Y coating case by 0.2–0.5 W m<sup>-2</sup> and TR-W coating case by 0.4–1.3 W m<sup>-2</sup>. Additionally, the NIR-Y coating case had the lowest building heat storage flux at only 33.4 W m<sup>-2</sup>, 6.0 W m<sup>-2</sup> less than the uncoated group, followed by TR-Y coating at 33.9 W m<sup>-2</sup> and TR-W coating at 36.9 W m<sup>-2</sup>.

### 3.3. Limitations and future work

We examined the impact of various cool coating materials (TR-W, TR-Y and NIR-Y coatings) on high-rise building clusters with two urban densities ( $\lambda_p = 0.25, 0.44$ ) across three coating modes, utilizing scaled outdoor experiments conducted from May 11 to July 12. For this research, ideal concrete models were employed, mirroring the building

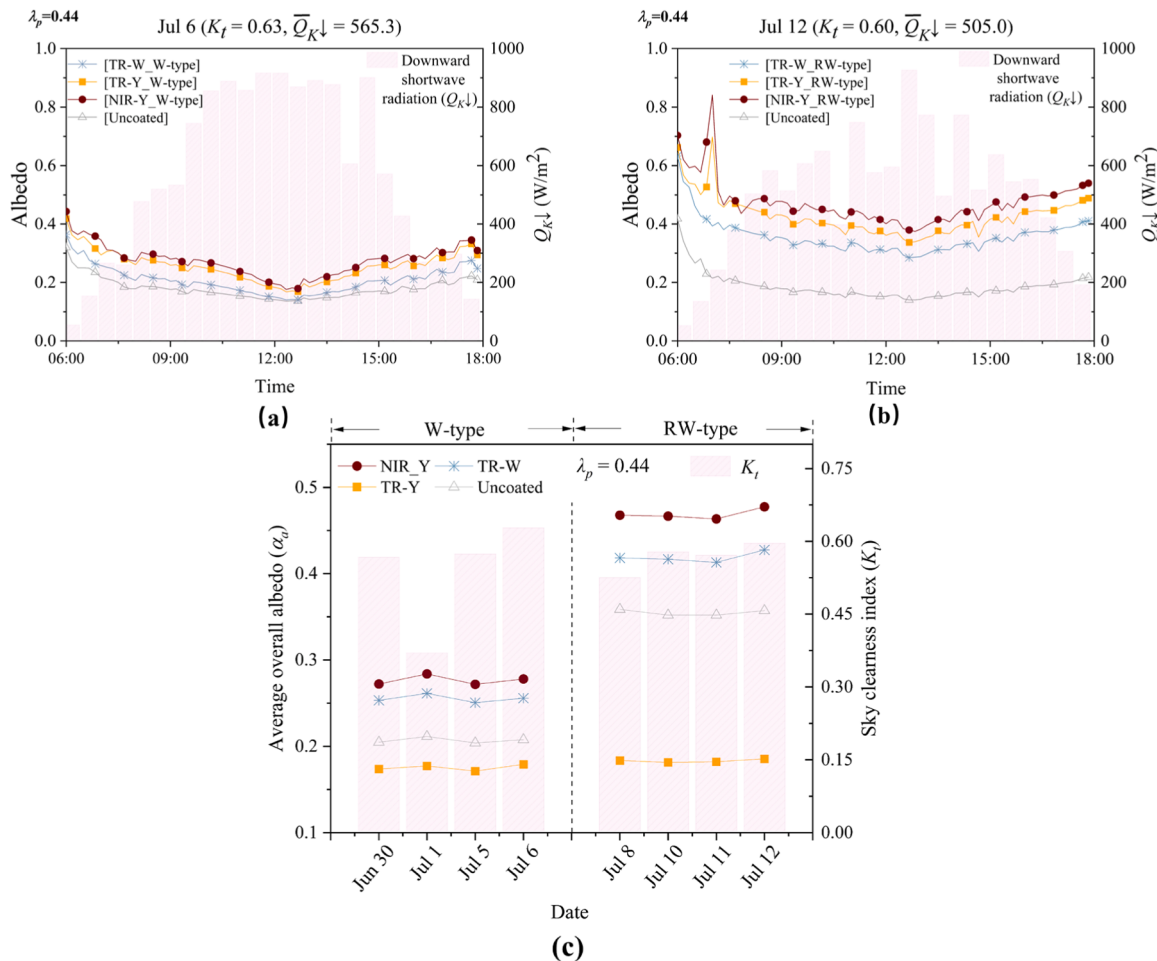


**Fig. 9.** Diurnal variations in overall albedo ( $\alpha_a$ ) and downward shortwave radiation ( $Q_{K\downarrow}$ ) for various cases with two coating modes and three coating materials (TR-W, TR-Y and NIR-Y coating) at  $\lambda_p = 0.44$  on two selected days (Jul 6, 12): (a) W-type, (b) RW-type, and (c) the variations of average overall albedo ( $\alpha_a$ ) and sky clearness index ( $K_t$ ) during the non-rainy days.

material and scale of real buildings but excluding primary building components like windows, doors, and ventilation systems. Our analysis focused on key metrics such as overall albedo, surface cooling, indoor air temperature, and heat storage flux, calculated by the Element Surface Temperature Method (ESTM). Despite potential oversights, like the absence of windows and building layering that might affect indoor thermal comfort parameters, these high-quality, parameterized experimental data are still invaluable for validating CFD simulations and SEB models (e.g., Zhang et al., 2019). The refined CFD and SEB models can subsequently be used to explore a broader array of full-scale urban districts or building clusters. In addition, we see great potential in utilizing machine learning approaches such as physics-informed neural networks (PINNs, Cuomo et al., 2022; Tehrani et al., 2024). By training these networks with years of field experiment data, we can explore how weather-related and building morphology-related parameters affect urban surface and air temperatures. This neural network approach aims to provide a faster and more efficient alternative to traditional numerical simulation methods (Liu et al., 2021; Xie et al., 2022).

Our current study focuses on typical urban models specifically designed for the summer season in a subtropical climate. However, the effectiveness of cooling coatings can vary across different climate zones. In future research, we will conduct a similar study in the temperate zone of northern China to enrich our experimental database, enabling a more comprehensive analysis of the impact of climate differences on the application of cooling coatings. Long-term monitoring is also among our research interests. We will also examine the annual and seasonal

variations of these effects, particularly the performance of cool coatings during winter and on rainy days.

Moreover, we aim to incorporate a wider selection of cool coating materials, such as cool coating mixed with phase change materials (PCM, Lei et al., 2017) and supercool materials with solar reflectance exceeding 0.9 (Santamouris et al., 2020), and to examine the influence of wall-to-window ratios on the coatings' indoor and outdoor cooling effects. Given the potential glare issues associated with the high-reflectance materials, future investigations will also consider utilize dark-colored cool coatings (Doya et al., 2012). Additionally, we will consider conducting sensitivity experiments on input parameters, such as the coverage ratio of coatings—applying the coating only at higher wall levels may reduce glare caused by highly reflective coatings while still achieving a cooling effect similar to that of full wall coverage. In scaled-down experiments, due to the controllability of other variables, we will be able to quantify the impact of single-variable changes on the building's wind and thermal environment. Furthermore, we plan to explore integrating cool coatings with other urban cooling strategies, such as green roofs/walls (Hang et al., 2024a; Wu et al., 2024; Zheng et al., 2024), to evaluate their combined cooling effects, as well as extending our research to high-rise structures to better understand vertical surface interactions with solar radiation.

Our experimental findings could provide reference for the validation of related simulation models. However, there are still many uncertainties regarding the application of new materials in urban renewal, such as cost, durability, and the potential impact on pedestrians. To fully

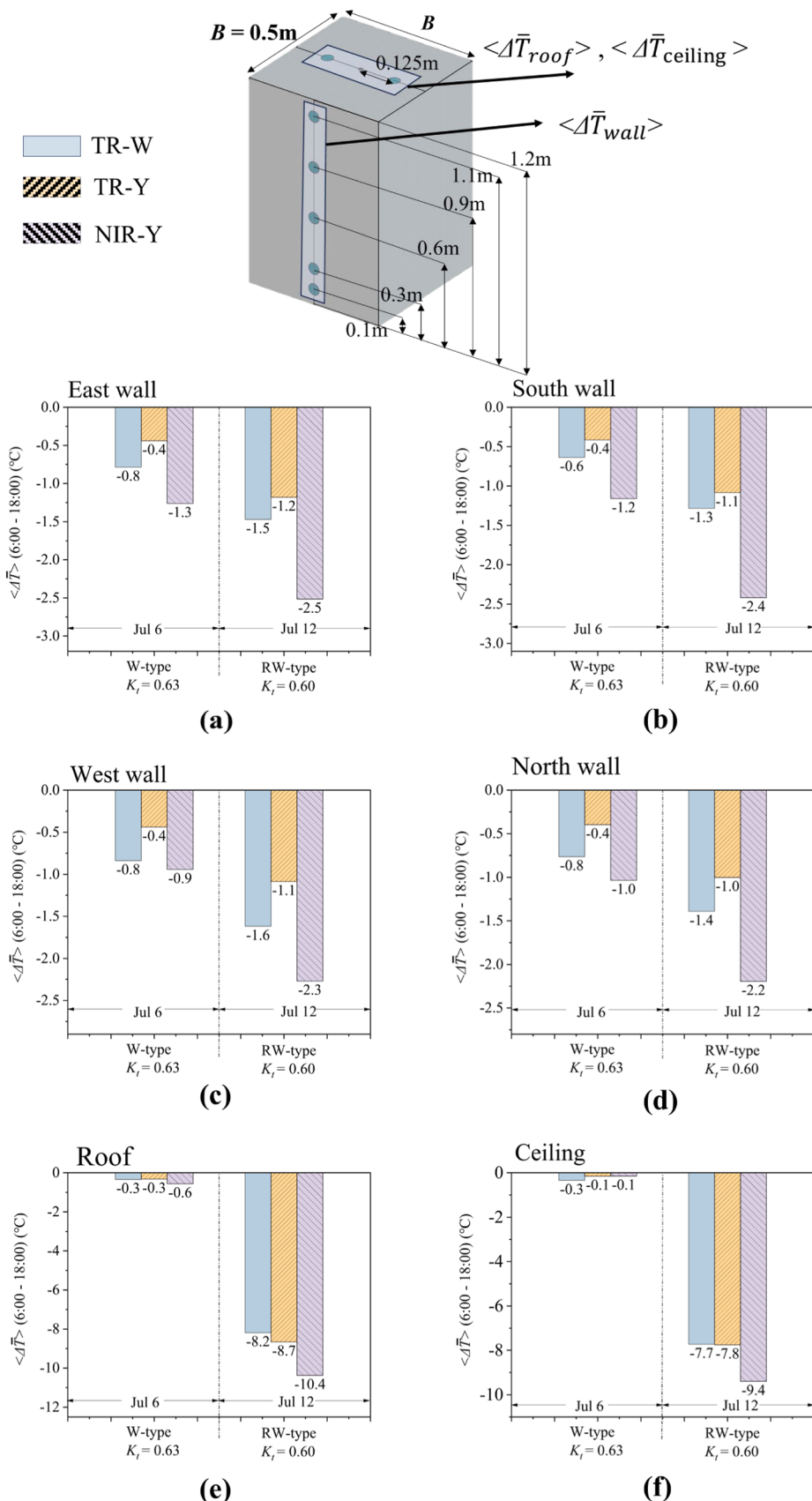


**Fig. 10.** Bar charts of  $\langle \Delta T_{wall} \rangle$ ,  $\langle \Delta T_{roof} \rangle$  and  $\langle \Delta T_{ceiling} \rangle$  from 6:00 to 18:00 between coated and uncoated cases with two coating modes (W-type, RW-type) and three coating materials (TR-W, TR-Y and NIR-Y coating) at  $\lambda_p = 0.44$  on two selected days (Jul 6, 12): (a) East wall, (b) South wall, (c) West wall, (d) North wall, (e) Roof, (f) Ceiling.

**Table 8**

Summary of the maximum coated building surface (wall, roof and ceiling) cooling ( $\langle \Delta T_{max} \rangle$ ) during daytime (6:00–18:00) for various cases at  $\lambda_p=0.44$  with different coating materials and coating modes.

Date	Case name	Variables	Maximum cooling ( $\Delta T_{max}$ ) (°C) $\langle \Delta T \rangle = \langle T_{Coated} \rangle - \langle T_{uncated} \rangle$					
			East wall	South wall	West wall	North wall	Roof	Ceiling
Jul 6, ( $K_t=0.63$ )	[TR-W_W-type]	Coating materials, W-type	-1.8	-1.3	-1.9	-2.0	-2.4	-1.9
	[TR-Y_W-type]		-1.6	-1.1	-1.6	-1.8	-5.0	-2.2
	[NIR-Y_W-type]		-3.0	-2.5	-2.5	-3.0	-3.5	-1.9
Jul 12, ( $K_t=0.60$ )	[TR-W_RW-type]	Coating materials, RW-type	-2.5	-2.0	-2.7	-2.4	-14.4	-13.5
	[TR-Y_RW-type]		-2.0	-1.8	-2.1	-2.2	-14.1	-12.3
	[NIR-Y_RW-type]		-4.0	-3.7	-3.7	-4.1	-17.3	-14.7

understand these factors, it would be reasonable to use validated numerical models to conduct targeted simulation experiments for each city.

#### 4. Conclusion

We conducted scaled outdoor experiments during the hot summer (May 11 - Jul 12, 2023) in Guangzhou, P.R. China, a typical subtropical monsoon climate area. The quantitative effect of building packing densities (plan and frontal area indexes  $\lambda_p = 0.25/0.44$  and  $\lambda_f = 0.6/1.06$ ), coating materials (traditional high-reflective white and yellow coating, TR-W and TR-Y (solar reflectance: 0.73, 0.76)), yellow near-infrared high-reflective coating, NIR-Y (solar reflectance: 0.76) and coating modes (R-type, W-type, RW-type) on the overall urban albedo ( $\alpha$ ), surface cooling, indoor and street air temperature and the building heat storage flux calculated by ESTM (the Element Surface Temperature Method) in 3D scaled high-rise building clusters (building height  $H = 1.2$  m, street width  $W = 0.5$  m/0.25 m).

For Period I, four partially cloudy days (May 15, 28, 29 and June 22) were selected for analysing the cooling effect of two building packing densities and three coating modes with the same TR-W material. The main findings are as below:

(1). All cool coating modes of R-type, W-type, RW-type significantly enhance overall average urban albedo ( $\alpha_a$ ) and models with  $\lambda_p = 0.44$  always experience greater  $\alpha_a$  than  $\lambda_p = 0.25$ . When  $\lambda_p = 0.25/0.44$ ,  $\alpha_a = 0.13/0.16$  in uncoated cases. Additionally, for models with  $\lambda_p = 0.25$  and 0.44, R-type coating increased  $\alpha_a$  by 84.6 % and 100.0 %, while RW-type coating raised them by 121.4 % and 125.0 %. In contrast, W-type coatings yielded a relatively modest increase in  $\alpha_a$  of 42.9 % and 17.6 %. Overall, as  $\lambda_p$  raised from 0.25 to 0.44,  $\alpha_a$  became much greater for R-type and RW-type but rose slightly for W-type due to the limited sky view factor and reduced incoming/outgoing solar radiation to the street.

(2). Greater building packing densities with narrower streets significantly reduce the side-wall cooling of high-reflective coatings under W-type and RW-type. At  $\lambda_p = 0.44$ , W-type coating achieved minimal cooling, reducing  $\Delta T_{wall}$  by only 0.6–0.8 °C. But with a larger sky view factor at  $\lambda_p = 0.25$ , the average cooling of street wall temperature was more pronounced, ranging from 2.3 to 2.7 °C. For RW-type coatings, the reduction of  $\Delta T_{wall}$  was 1.1–1.6 °C at  $\lambda_p = 0.44$ , while it increased to 3.8–4.4 °C at  $\lambda_p = 0.25$ . Additionally, both R-type and RW-type coatings substantially cooled down the internal(ceiling) and external roof surface by an average of 7–10 °C and a maximum of about 17 °C. However, building area densities of  $\lambda_p = 0.25$  and 0.44 experienced similar  $\Delta T_{wall}$  under R-type and W-type, whereas RW-type showed an average cooling increase of 1.6–2.2 °C at  $\lambda_p = 0.25$ .

(3). The cooling effect of wall coatings on indoor air diminishes with higher building area density and reduced internal height. At  $\lambda_p = 0.25$ , W-type and RW-type cases exhibited an average cooling of 2.3 °C and 3.8 °C for the entire indoor space, respectively, while dropping to 0.7 °C and 1.6 °C at  $\lambda_p = 0.44$ . In contrast to lower layers ( $z = 0.3, 0.1$  m), the  $\Delta T_{indoor\_air}$  in the upper layers (averaged of two heights  $z = 1.1, 0.9$  m) were much greater, i.e. 5.1 °C/3.1 °C at  $\lambda_p = 0.25/0.44$  for RW-type, and 2.6 °C/1.2 °C at  $\lambda_p = 0.25/0.44$  for W-type. These values were 2.5 °C/0.2 °C and 1.9 °C/0.1 °C at the lower layer ( $z = 0.3, 0.1$  m). For R-type, the indoor air temperature decreased mainly in the upper layers (by 2.0 °C) with only a slight reduction in the lower levels (by 0.6 °C), and this effect was minimally influenced by building area densities. The street air temperature variations for both the coated and uncoated groups were largely comparable, with the average temperature difference  $\langle \Delta T_{street\_air} \rangle$  (6:00–18:00) at  $\lambda_p = 0.25$  under W-type and RW-type was 0.6–0.8 °C lower than at  $\lambda_p = 0.44$ .

(4). High-reflectance coatings can moderately reduce the heat storage flux density on sidewalls and roofs. However, these effects are minor compared to the significant reductions in flux (6.3–11.0 W m<sup>-2</sup>) achieved by altering building area density.

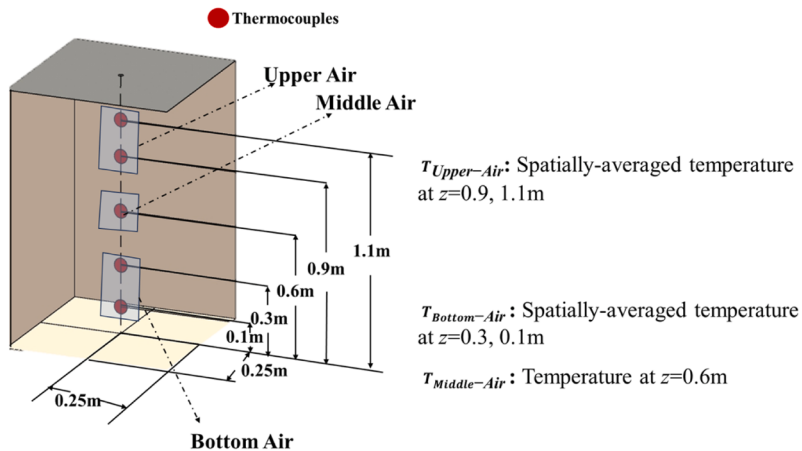
We also present a comparison of the cooling effects between high-reflective coatings of NIR-Y and TR-Y, TR-W under different coating modes (W-type, RW-type) at  $\lambda_p = 0.44$  on two selected partially cloudy days (July 6 and 12) with similar sky clearness index ( $K_t = 0.60, 0.63$ ).

(1). Under W-type and RW-type coatings, all three cool materials increase overall urban albedo ( $\alpha_a$ ), and the NIR-Y coating exhibits the greatest. Compared to uncoated cases with  $\alpha_a$  of 0.18–0.19, TR-W, TR-Y and NIR-Y coatings achieved greater  $\alpha_a$  of 0.21, 0.26, and 0.28 for W-type (increased by 16.0 %, 42.9 %, and 53.5 %, respectively), and 0.36, 0.43, and 0.47 for RW-type (compared to 0.19, increased by 89.5 %, 126.3 %, and 147.4 %, respectively). Three kinds of cool material produced similar building heat storage flux ( $\Delta Q_s$ ).

(2). NIR-Y coating attains greater cooling effect of building surfaces (side walls or roofs) than TR-Y and TR-W coatings. For instance, NIR-Y coating achieved a reduction in side-wall temperature of 0.9–1.3 °C for W-type and 2.2–2.5 °C for RW-type, which was approximately 2.25–3.25 times for W-type and 2.08–2.2 times for RW-type compared to the TR-Y coating (0.4 °C/1.0–1.2 °C). For RW-type, NIR-Y coating could achieve a roof cooling of 10.4 °C, which was an increase of approximately 26.83 % compared to TR-W (8.2 °C).

(3). NIR-Y coating achieves greater indoor-air average cooling by 0.5–1.2 °C compared to TR-Y and TR-W coatings. For instance, in W-type cases, NIR-Y (1.4 °C) coating produced approximately 1.75 times the indoor cooling effect of TR-W (0.8 °C) coatings. For RW-type, the NIR-Y coating provided an average upper-level cooling of 5 °C, significantly greater than that of TR-Y (3.6 °C) and TR-W coatings (3 °C).

The detailed findings offer valuable insights into using high-reflective cool coatings in three-dimensional high-rise building clusters at various building area densities to enhance indoor comfort, reduce urban surface temperatures, and mitigate urban heat islands. Additionally, we provide quantification of the cooling benefits of using NIR



**Indoor air temperature difference between coated and uncoated cases :**  $\Delta T_{indoor\_air} = \Delta T_{coated} - \Delta T_{uncoated}$

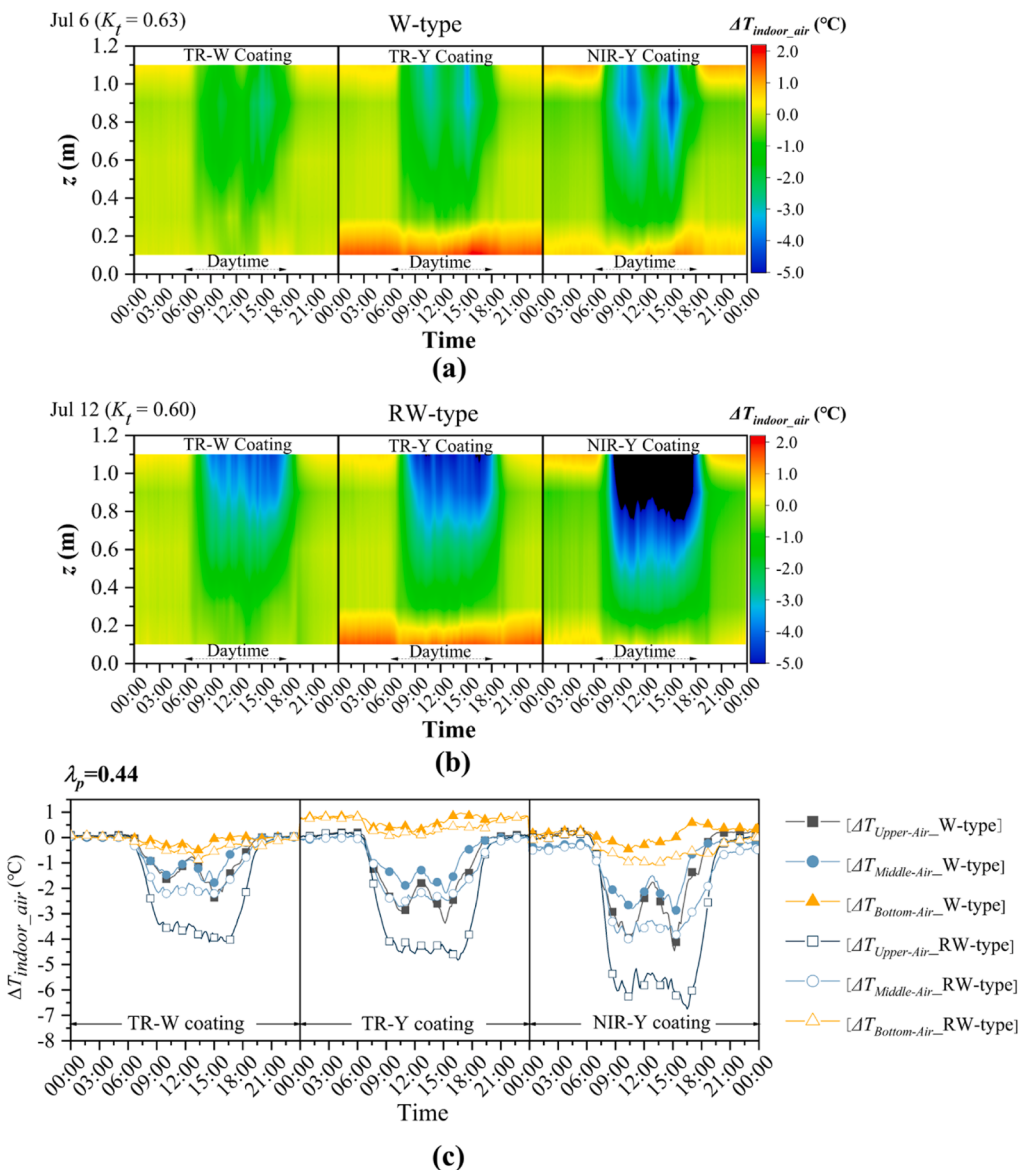


**Fig. 11.** Heatmap of indoor air temperature difference  $\Delta T_{indoor\_air}$  at different heights ( $z = 1.1, 0.9, 0.6, 0.3$  and  $0.1\text{ m}$ ) between coated and uncoated cases with two coating modes (W-type, RW-type) and three coating materials (TR-W, TR-Y and NIR-Y coating) at  $\lambda_p = 0.44$  on two selected days (Jul 6, 12): (a) W-type,  $K_t = 0.63$ , (b) RW-type,  $K_t = 0.60$ , and (c) the corresponding diurnal variations of  $\langle \Delta T_{indoor\_air} \rangle$  across three level (Upper-, Middle- and Bottom-air).

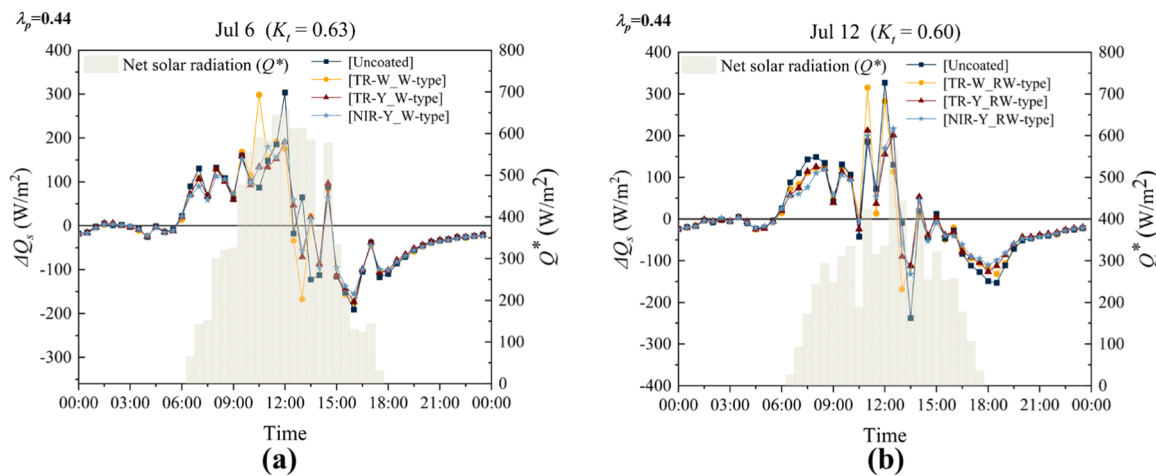


**Fig. 12.** Diurnal variations of the coated and uncoated building heat storage flux  $\Delta Q_s$  (calculated by the ESTM) and the net solar radiation  $Q^*$  for various cases with two coating modes (W-type, RW-type) and three coating materials (TR-W, TR-Y and NIR-Y coating) at  $\lambda_p = 0.44$  on two selected days (Jul 6, 12): (a) W-type,  $K_t = 0.63$ , (b) RW-type,  $K_t = 0.60$ .

**Table 9**

Summary of averaged and maximum energy fluxes of  $Q^*$ ,  $\Delta Q_s$  (calculated by ESTM), and averaged heat storage flux density during daytime (6:00–18:00) for various cases with different coating materials and coating modes at  $\lambda_p=0.44$ .

Date	Case name	$\Delta Q_{s,\max}$ ( $\text{W m}^{-2}$ )	$\Delta Q_{s,\text{avg}}$ ( $\text{W m}^{-2}$ )	$Q^*_{\max}$ ( $\text{W m}^{-2}$ )	$Q^*_{\text{avg}}$ ( $\text{W m}^{-2}$ )	Averaged heat storage flux density ( $\text{W m}^{-2}$ ) (6:00–18:00)							
						East wall	South wall	West wall	North wall	Roof	Ground	Indoor air	Street air
Jul 6, ( $K_t=0.63$ )	[Uncoated]	303.6	32.5	655.7	356.2	3.9	3.9	4.1	4.4	2.2	13.7	0.1	0.1
	[TR-W_W-type]	298.2	33.3			3.8	3.7	3.8	3.9	2.2	15.6	0.1	0.1
	[TR-Y_W-type]	191.0	31.3			3.6	3.6	3.8	3.8	2.3	14.0	0.1	0.1
	[NIR-Y_W-type]	191.7	32.9			3.8	3.8	3.9	3.9	2.4	15.0	0.1	0.1
Jul 12, ( $K_t=0.60$ )	[Uncoated]	326.9	39.4	564.7	252.4	5.2	5.2	5.8	6.0	3.4	13.5	0.1	0.1
	[TR-W_RW-type]	315.2	36.9			4.6	4.6	5.0	5.0	2.6	14.8	0.1	0.1
	[TR-Y_RW-type]	212.3	33.9			4.3	4.3	4.8	4.8	2.4	12.9	0.1	0.1
	[NIR-Y_RW-type]	216.6	33.4			4.1	4.1	4.4	4.3	2.2	14.0	0.1	0.1

coatings in subtropical climates and comparisons with TR coatings. These results can also support the validation of numerical models, facilitating improvements and broader application of numerical simulations at both urban and block scales.

#### CRediT authorship contribution statement

**Jian Hang:** Writing – review & editing, Writing – original draft, Visualization, Validation, Supervision, Resources, Project administration, Methodology, Funding acquisition, Formal analysis, Conceptualization. **Mengrong Lu:** Writing – review & editing, Writing – original draft, Visualization, Validation, Software, Methodology, Investigation, Formal analysis, Data curation, Conceptualization. **Longhao Ren:** Software, Formal analysis, Data curation. **Hanying Dong:** Resources, Formal analysis, Data curation. **Yuguang Zhao:** Formal analysis, Data curation. **Na Zhao:** Formal analysis, Data curation.

#### Declaration of competing interest

The authors declare that they have no known competing financial interests or personal relationships that could have appeared to influence the work reported in this paper.

#### Acknowledgments

This study was financially supported by National Natural Science Foundation of China (No. U2442212 and 42175095), Innovation Group Project of Southern Marine Science and Engineering Guangdong Laboratory (Zhuhai) (No. 311020001), Fundamental Research Funds for the Central Universities, Sun Yat-sen University (No: 24xkj004).

#### Supplementary materials

Supplementary material associated with this article can be found, in the online version, at [doi:10.1016/j.scs.2025.106200](https://doi.org/10.1016/j.scs.2025.106200).

#### Data availability

The data that has been used is confidential.

#### References

- Aida, M. (1982). Urban albedo as a function of the urban structure - a model experiment. *Boundary Layer Meteorology*, 23(4), 405–413.
- Assunção, H. F., Escobedo, J. F., & Oliveira, A. P. D. (2007). A new algorithm to estimate sky condition based on 5 minutes-averaged values of clearness index and relative optical air mass. *Theoretical and Applied Climatology*, 90, 235–248.

- Becherini, F., Lucchi, E., Gandini, A., Barrasa, M. C., et al. (2018). Characterization and thermal performance evaluation of infrared reflective coatings compatible with historic buildings. *Building and Environment*, 134, 35–46.
- Chen, G., Wang, D., Wang, Q., Li, Y., et al. (2020a). Scaled outdoor experimental studies of urban thermal environment in street canyon models with various aspect ratios and thermal storage. *Science of the Total Environment*, 726, Article 138147.
- Chen, G., Yang, X., Yang, H., Hang, J., et al. (2020b). The influence of aspect ratios and solar heating on flow and ventilation in 2D street canyons by scaled outdoor experiments. *Building and Environment*, 185, Article 107159.
- Chen, J., & Lu, L. (2021a). Comprehensive evaluation of thermal and energy performance of radiative roof cooling in buildings. *Journal of Building Engineering*, 33, Article 101631.
- Chen, J., Lu, L., Gong, Q., Wang, B., et al. (2021b). Development of a new spectral selectivity-based passive radiative roof cooling model and its application in hot and humid region. *Journal of Cleaner Production*, 307, Article 127170.
- Chen, T., Yang, H., Chen, G., Lam, C. K. C., et al. (2021). Integrated impacts of tree planting and aspect ratios on thermal environment in street canyons by scaled outdoor experiments. *Science of the Total Environment*, 764, Article 142920.
- Coser, E., Moritz, V. F., Krenzinger, A., & Ferreira, C. A. (2015). Development of paints with infrared radiation reflective properties. *Polímeros*, 25, 305–310.
- Cuomo, S., Di Cola, V. S., Giampaolo, F., Rozza, G., et al. (2022). Scientific machine learning through physics-informed neural networks: Where we are and what's next. *Journal of Scientific Computing*, 92(3), 88.
- Djafer, D., Irbah, A., & Zaiani, M. (2017). Identification of clear days from solar irradiance observations using a new method based on the wavelet transform. *Renewable Energy*, 101, 347–355.
- Donateo, A., Palusci, O., Pappacogli, G., Esposito, A., et al. (2023). Analysis of urban heat island and human thermal comfort in a Mediterranean city: A case study of Lecce (Italy). *Sustainable Cities and Society*, 98, Article 104849.
- Donthu, E. K. K., Long, Y. P., Wan, M. P., Zhou, M., et al. (2024). Dynamics of cool surface performance on urban microclimate: A full-scale experimental study in Singapore. *Sustainable Cities and Society*, 102, Article 105218.
- Doya, M., Bozonnet, E., & Allard, F. (2012). Experimental measurement of cool facades' performance in a dense urban environment. *Energy and Buildings*, 55, 42–50.
- Duffie, J.A., Beckman, W.A., 2013. Solar engineering of thermal processes (p. 910). John Wiley & Sons.
- Family, R., & Mengüç, M. P. (2017). Materials for radiative cooling: A review. *Procedia Environmental Sciences*, 38, 752–759.
- Feng, J., Khan, A., Doan, Q. V., Gao, K., et al. (2021). The heat mitigation potential and climatic impact of super-cool broadband radiative coolers on a city scale. *Cell Reports Physical Science*, 2(7).
- Garg, V., Kotharkar, R., Sathaye, J., & Rallapalli, H. (2016). Assessment of the impact of cool roofs in rural buildings in India. *Energy and Buildings*, 114, 156–163.
- Grimmond, C. S. B., & Oke, T. R. (1999). Heat storage in urban areas: Local-scale observations and evaluation of a simple model. *Journal of Applied Meteorology*, 38(7), 922–940.
- Hang, J., An, L., Zhao, Y., Wu, Z., et al. (2024a). Comparative simulation of transpiration and cooling impacts by porous canopies of shrubs and trees. *Sustainable Cities and Society*, Article 105573.
- Hang, J., & Chen, G. (2022). Experimental study of urban microclimate on scaled street canyons with various aspect ratios. *Urban Climate*, 46, Article 101299.
- Hang, J., Shi, Y., & Zeng, L. (2024b). Seasonal and diurnal urban energy balance and carbon exchanges over a residential neighborhood in a humid subtropical city. *Urban Climate*, 53, Article 101774.
- He, Y., Yu, H., Ozaki, A., & Dong, N. (2020). Thermal and energy performance of green roof and cool roof: A comparison study in Shanghai area. *Journal of Cleaner Production*, 267, 122205.
- Huang, D. Y., Xu, Y. G., Sun, C. X., Deng, H. M., et al. (2010). Distribution, regional sources and deposition fluxes of organochlorine pesticides in precipitation in Guangzhou, South China. *Atmospheric Research*, 97(1-2), 115–123.
- Jacobson, M. Z., & Ten Hoeve, J. E. (2012). Effects of urban surfaces and white roofs on global and regional climate. *Journal of Climate*, 25(3), 1028–1044.
- Jiang, L., Gao, Y., Zhuang, C., Feng, C., et al. (2023). Experimental and numerical study on thermal performance of phase-change-material cool roofs in summer. *Sustainable Cities and Society*, 99, Article 104936.
- Kanda, M. (2006). Progress in the scale modeling of urban climate: review. *Theoretical and Applied Climatology*, 84(1-3), 23–33.
- Kawai, T., & Kanda, M. (2010). Urban energy balance obtained from the comprehensive outdoor scale model experiment. Part I: basic features of the surface energy balance. *Journal of Applied Meteorology and Climatology*, 49(7), 1341–1359.
- Kim, G. A., Song, B. G., & Park, K. H. (2020). Long-term monitoring for comparison of seasonal effects on cool roofs in humid subtropical climates. *Energy and Buildings*, 206, 109572.
- Lei, J., Kumarasamy, K., Zingre, K. T., Yang, J., et al. (2017). Cool colored coating and phase change materials as complementary cooling strategies for building cooling load reduction in tropics. *Applied Energy*, 190, 57–63.
- Li, Q., Zhang, X., & Hang, J. (2024). Numerical investigations of cool coatings on building envelopes for urban heat mitigation with various street aspect ratios. *Sustainable Cities and Society*, 107, Article 105410.
- Liu, B. Y., & Jordan, R. C. (1960). The interrelationship and characteristic distribution of direct, diffuse and total solar radiation. *Solar Energy*, 4(3), 1–19.
- Liu, S., Zhang, J., Li, J., Li, Y., et al. (2021). Simulating and mitigating extreme urban heat island effects in a factory area based on machine learning. *Building and Environment*, 202, Article 108051.
- Lu, M., Zeng, L., Li, Q., Hang, J., et al. (2023). Quantifying cooling benefits of cool roofs and walls applied in building clusters by scaled outdoor experiments. *Sustainable Cities and Society*, 97, Article 104741.
- Morini, E., Castellani, B., Presciutti, A., Anderini, E., et al. (2017). Experimental analysis of the effect of geometry and façade materials on urban district's equivalent albedo. *Sustainability*, 9(7), 1245.
- Morini, E., Castellani, B., De Ciantis, S., Anderini, E., et al. (2018). Planning for cooler urban canyons: Comparative analysis of the influence of façades reflective properties on urban canyon thermal behavior. *Solar Energy*, 162, 14–27.
- Nazarian, N., Dumas, N., Kleissl, J., & Norford, L. (2019). Effectiveness of cool walls on cooling load and urban temperature in a tropical climate. *Energy and Buildings*, 187, 144–162.
- Offerle, B., Grimmond, C. S. B., & Fortuniak, K. (2005). Heat storage and anthropogenic heat flux in relation to the energy balance of a central European city centre. *International Journal of Climatology: A Journal of the Royal Meteorological Society*, 25 (10), 1405–1419.
- Oke, T. R. (1988). The urban energy balance. *Progress in Physical Geography*, 12(4), 471–508.
- Oke, T. R., Johnson, D. G., Steyn, D. G., & Watson, I. D. (1991). Simulation of surface urban heat island under 'ideal' conditions at night – part 2: Diagnosis and causation. *Boundary-Layer Meteorology*, 56, 339–358.
- Paravantis, J., Santamouris, M., Cartalis, C., Efthymiou, C., et al. (2017). Mortality associated with high ambient temperatures, heatwaves, and the urban heat island in Athens, Greece. *Sustainability*, 9(4), 606.
- Pearlmutter, D., Berliner, P., & Shaviv, E. (2006). Physical modeling of pedestrian energy exchange within the urban canopy. *Building and Environment*, 41(6), 783–795.
- Pearlmutter, D., Berliner, P., & Shaviv, E. (2007). Integrated modeling of pedestrian energy exchange and thermal comfort in urban street canyons. *Building and Environment*, 42, 2396–2409.
- Pisello, A. L., Rossi, F., & Cotana, F. (2014). Summer and winter effect of innovative cool roof tiles on the dynamic thermal behavior of buildings. *Energies*, 7(4), 2343–2361.
- Pisello, A. L., Castaldo, V. L., Pignatta, G., Cotana, F., et al. (2016). Experimental in-lab and in-field analysis of waterproof membranes for cool roof application and urban heat island mitigation. *Energy and Buildings*, 114, 180–190.
- Pisello, A. L. (2017). State of the art on the development of cool coatings for buildings and cities. *Solar Energy*, 144, 660–680.
- Prado, R. T. A., & Ferreira, F. L. (2005). Measurement of albedo and analysis of its influence on the surface temperature of building roof materials. *Energy and Buildings*, 37 (4), 295–300.
- Raman, A. P., Anoma, M. A., Zhu, L., Rephaeli, E., et al. (2014). Passive radiative cooling below ambient air temperature under direct sunlight. *Nature*, 515(7528), 540–544.
- Revel, G. M., Martarelli, M., Emiliani, M., Gozalbo, A., et al. (2014). Cool products for building envelope—Part I: Development and lab scale testing. *Solar Energy*, 105, 770–779.
- Revel, G. M., Martarelli, M., Emiliani, M., Celotti, L., et al. (2014a). Cool products for building envelope—Part II: Experimental and numerical evaluation of thermal performances. *Solar Energy*, 105, 780–791.
- Rincón, L., Gangolells, M., Medrano, M., & Casals, M. (2024). Climate change mitigation and adaptation in Spanish office stock through cool roofs. *Energy and Buildings*, 323, Article 114738.
- Santamouris, M. (2015). Analyzing the heat island magnitude and characteristics in one hundred Asian and Australian cities and regions. *Science of the Total Environment*, 512, 582–598.
- Santamouris, M. (2015a). Regulating the damaged thermostat of the cities—Status, impacts and mitigation challenges. *Energy and Buildings*, 91, 43–56.
- Santamouris, M. (2016). Innovating to zero the building sector in Europe: Minimising the energy consumption, eradication of the energy poverty and mitigating the local climate change. *Solar Energy*, 128, 61–94.
- Santamouris, M., Symnefa, A., & Karlessi, T. (2011). Using advanced cool materials in the urban built environment to mitigate heat islands and improve thermal comfort conditions. *Solar Energy*, 85(12), 3085–3102.
- Santamouris, M., & Yun, G. Y. (2020). Recent development and research priorities on cool and super cool materials to mitigate urban heat island. *Renewable Energy*, 161, 792–807.
- Snyder, W. H. (1972). Similarity criteria for the application of fluid models to the study of air pollution meteorology. *Boundary Layer Meteorology*, 3(1), 113–134.
- Syafii, N. I., Ichinose, M., Kumakura, E., Jusuf, S. K., et al. (2017). Thermal environment assessment around bodies of water in urban canyons: A scale model study. *Sustainable Cities and Society*, 34, 79–89.
- Taha, H., Sailor, D. J., Alkbari, H., 1992. High-albedo materials for reducing building cooling energy use. CA United States: Lawrence Berkeley Lab.
- Tehrani, A. A., Veisi, O., Fakhr, B. V., & Du, D. (2024). Predicting solar radiation in the urban area: A data-driven analysis for sustainable city planning using artificial neural networking. *Sustainable Cities and Society*, 100, Article 105042.
- United Nations Human Settlements Programme (UN-Habitat), 2020. *World cities report 2020: the value of sustainable urbanization*. Nairobi, Kenya: United Nations Human Settlements Programme (UN-Habitat). ISBN 978-92-1-0054386.
- Wang, D., Shi, Y., Chen, G., Zeng, L., et al. (2021). Urban thermal environment and surface energy balance in 3D high-rise compact urban models: Scaled outdoor experiments. *Building and Environment*, 205, Article 108251.
- Wang, H., Hang, J., Yang, J., Gao, Z., et al. (2024). Reduced-scale experimental study on the cooling effect of solar control films and cool materials. *Energy and Buildings*, 320, Article 114636.
- Wang, J., Liu, S., Liu, Z., Meng, X., et al. (2022). An experimental comparison on regional thermal environment of the high-density enclosed building groups with retro-reflective and high-reflective coatings. *Energy and Buildings*, 259, Article 111864.

- Wu, Z., Shi, Y., Ren, L., & Hang, J. (2024). Scaled outdoor experiments to assess impacts of tree evapotranspiration and shading on microclimates and energy fluxes in 2D street canyons. *Sustainable Cities and Society*, 108, Article 105486.
- Xie, Y., Ishida, Y., Hu, J., & Mochida, A. (2022). Prediction of mean radiant temperature distribution around a building in hot summer days using optimized multilayer neural network model. *Sustainable Cities and Society*, 84, Article 103995.
- Xu, F., Zhang, J. J., Gao, Z., Tian, D., et al. (2023). Study on the energy-saving effects of radiative material properties and material coating ratios in residential neighborhoods with different morphologies. *Energy and Buildings*, 301, Article 113718.
- Xu, F., Hang, J., Wang, H., Gao, Z., et al. (2024). An experimental study of the effects of using cool materials at different building heights on the indoor and outdoor environment. *Building and Environment*, 259, Article 111664.
- Yang, L., & Li, Y. (2009). City ventilation of Hong Kong at no-wind conditions. *Atmospheric Environment*, 43(19), 3111–3121.
- Zhang, K., Chen, G., Wang, X., Liu, S., et al. (2019). Numerical evaluations of urban design technique to reduce vehicular personal intake fraction in deep street canyons. *Science of the Total Environment*, 653, 968–994.
- Zhang, L., Luo, F., Pan, G., Zhang, W., et al. (2024). Elucidating the multi-timescale variability of a canopy urban heat island by using the short-time Fourier transform. *Geophysical Research Letters*, 51(1), Article e2023GL106221. Article.
- Zhang, N., Chen, Y., Luo, L., & Wang, Y. (2017). Effectiveness of different urban heat island mitigation methods and their regional impacts. *Journal of Hydrometeorology*, 18(11), 2991–3012.
- Zheng, X., Hu, W., Luo, S., Chen, J., et al. (2024). A scaled outdoor experimental study of the urban thermal environment in street canyons with green walls under various weather conditions. *Sustainable Cities and Society*, 105, Article 105310.
- Zingre, K. T., Wan, M. P., Tong, S., Li, H., et al. (2015). Modeling of cool roof heat transfer in tropical climate. *Renewable Energy*, 75, 210–223.